Moving measurements

Measurements on the turbulent/non-turbulent interface of a round jet in a co-moving frame of reference

C.V.B. Been

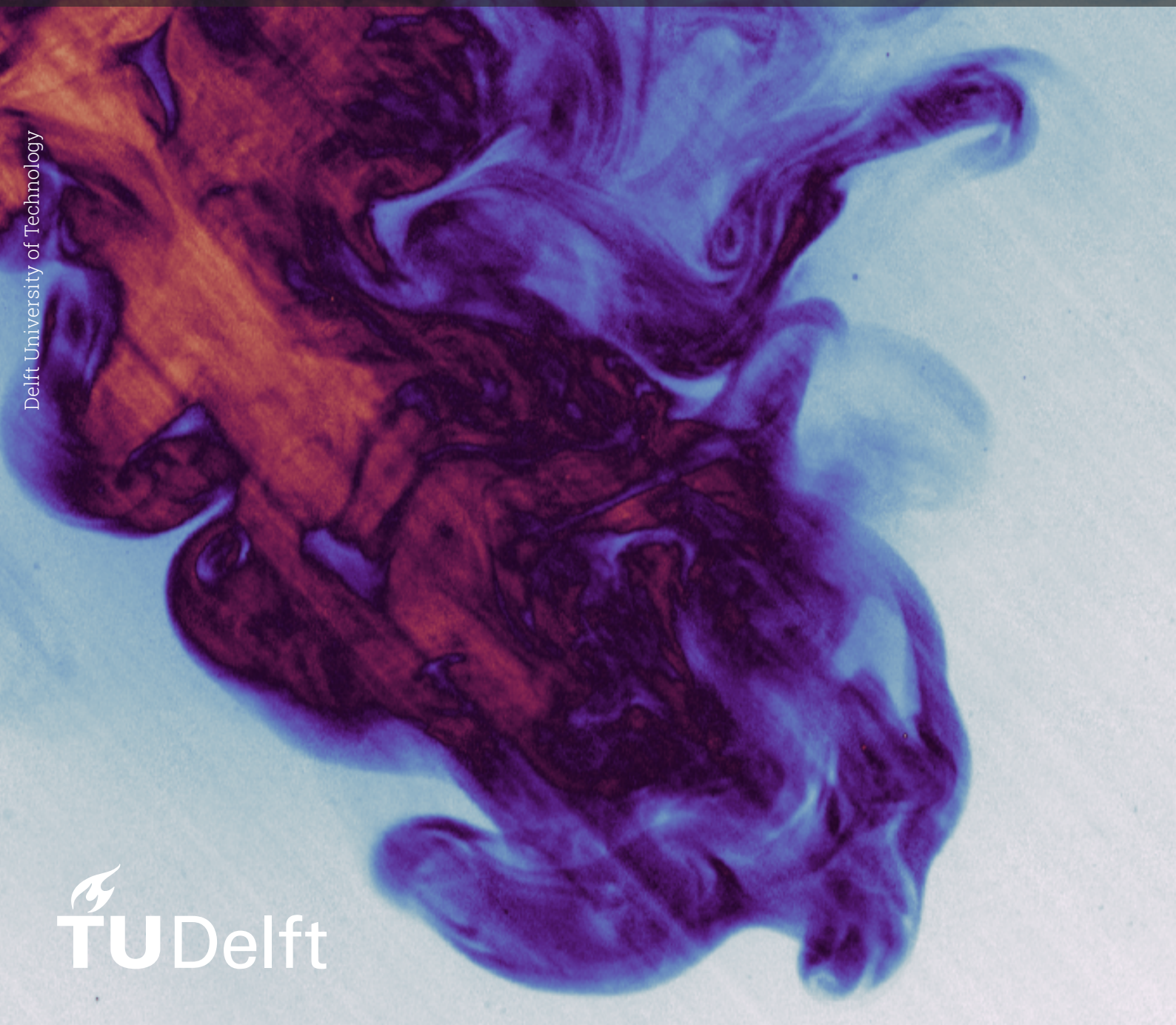

Delft University of Technology

TU Delft

Moving measurements

Measurements on the turbulent/non-turbulent interface of a round jet in a co-moving frame of reference

by

C.V.B. Been

to obtain the degree of Master of Science
at the Delft University of Technology,
to be defended publicly on Wednesday March 27, 2024 at 15:00.

Student number: 4575164

Thesis committee:	Prof. dr. ir. J. Westerweel,	TU Delft, supervisor
	Ir. L.E. van Dalen,	TU Delft, supervisor
	Dr. ir. A.R. Khojasteh,	TU Delft, supervisor
	Dr. ir. J.W.R. Peeters,	TU Delft, committee member

TU Delft

Abstract

At the turbulent/non-turbulent interface (TNTI) of a jet flow, momentum is transferred from the turbulent jet fluid to the fluid at rest. This transfer is governed by two mechanisms. One of them is related to the large scales of the flow and the other relates to the small scales of the flow. Which of the two is dominant is still a point of discussion. To analyse the TNTI the instantaneous information of the flow and the location of the interface is of great importance. However, the interface simultaneously develops and travels downstream from the nozzle. With stationary measurement techniques this limits the number of frames the interface can be seen developing as it travels in and out of the FOV. In this thesis the TNTI is measured using a camera system that moves along with the TNTI to get high resolution instantaneous measurements of the same part of the evolving interface. The measurement techniques that are used for this experiment are Particle Image Velocimetry (PIV) and Laser Induced Fluorescence (LIF). The cameras for these measurements are mounted to a motorised frame to keep the same part of the interface in view of the cameras as it develops.

Three Reynolds numbers are measured with this setup and the cameras move approximately $50D_n$ at a velocity close to the velocity of the interface along a diagonal path to follow the evolution of the TNTI.

One measurement with a Reynolds number of approximately 1.2×10^4 has been processed to show the quality of the results that can be obtained from such a measurement. The velocities are computed by an in-house interrogation analysis program in MATLAB to overcome the wide range of particle displacement found in this experiment, due to the presence of both the centreline and the TNTI of the jet. The TNTI is detected using the LIF data and a threshold detection method from literature that determines a threshold value. The results from the PIV and LIF processing is combined to compute the average conditional vorticity over the interface.

The results show that the PIV analysis is able to compute the velocities of almost the entire jet. Only showing a lot of spurious vectors close to the nozzle in the core of the jet. The LIF edge detection algorithm, on the other hand, does not perform as expected. In multiple instances, an internal interface is detected instead of the TNTI. The TNTI is also determined by identifying a threshold value through a visual inspection of the LIF images. This manually determined TNTI is used as a point of comparison for the average conditional vorticity profiles. The average conditional vorticity profiles support the conclusion that an interface internal to the jet is detected when comparing the interface from the algorithm to the interface determined manually.

Although not quantified in this thesis, there are moving measurements that show the same section of the TNTI evolving for many frames. This gives the co-moving measurements a clear advantage in measurement time compared to stationary measurements when trying to measure the moving TNTI. Refinements to the experimental setup, the behaviour of these internal interfaces and the detection of the TNTI can be of interest for future research.

Scan the QR code to see a movie of the measurements.

Contents

1

Introduction

When fluid is injected into another body of fluid at rest, it forms what is known as a jet flow [1]. From the moment the jet fluid enters the quiescent fluid, the turbulent jet fluid and non-turbulent surrounding fluid start to mix. During this mixing process, momentum from the turbulent jet is transferred to the non-turbulent fluid, which is drawn into the turbulent jet. So, the region that constitutes the jet increases in size as the fluid travels further from the injection point.

Turbulent flow is rotational as it carries vorticity [1], while the fluid which is originally at rest does not. The transfer of momentum happens at the interface between the rotational and irrotational regions. This interface is referred to as the Turbulent/Non-turbulent interface (TNTI) [2]. Figure 1.1 shows a frame of the experiment with the TNTI highlighted by a white line. At the interface, the non-turbulent fluid can be made turbulent in two ways.

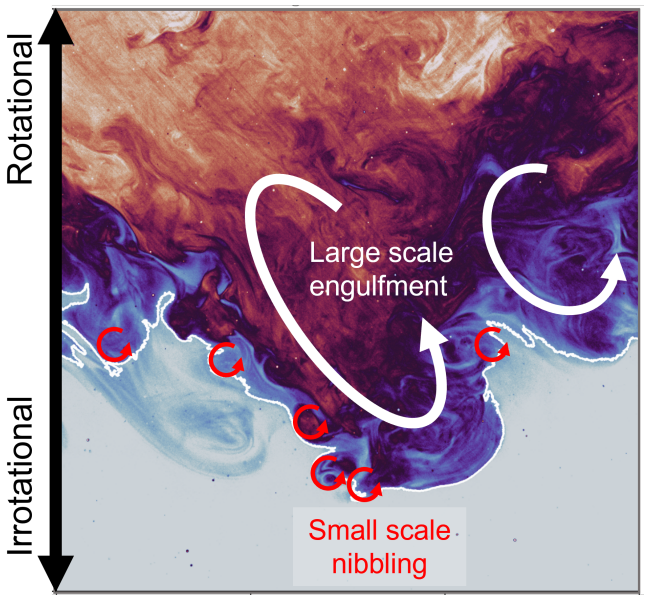

Figure 1.1: The border between the turbulent and non-turbulent regions is drawn in white. The irrotational fluid is made rotational by large-scale engulfment and small-scale nibbling.

The external fluid is drawn into the jet by engulfment at large scales. This is a largely inviscid process where external fluid is surrounded by turbulent jet fluid that moves first outward from the interface and then back toward the jet [2].

At the small scales it is a process called nibbling that is responsible for the increase in volume of turbulent fluid. Nibbling is a partially viscous process where the interface moves outward because of the irregular eddy motion near the TNTI [2].

Which of the two mechanisms is the dominant process is still undecided. Results from older studies have shown that engulfment is largely responsible for entrainment. However, more recent studies claim that entrainment is dominated by the small-scale nibbling process [3, 4].

To get more insight into the mechanisms at play, the evolution of the TNTI must be studied in more detail. However, the TNTI is simultaneously evolving and moving downstream. The movement of the interface limits the time the TNTI can be observed with stationary tools.

1.1. Aim of the research

The aim of the research is to perform measurements in a co-moving frame to get high resolution instantaneous measurements of the same section of the TNTI, in order to study the interface evolution and to get a better understanding of the mechanisms responsible for jet entrainment.

These measurements frame are performed on the turbulent/non-turbulent interface (TNTI) of a round jet seeded with particles and fluorescent dye. These measurements are performed in a water tunnel using Particle Image Velocimetry (PIV) and Laser Induced Fluorescence (LIF). PIV is used to measure the fluid velocity by imaging particles in the flow and will result in a vector field of the instantaneous velocity for each frame. LIF is used to measure the concentration of the dye and will be used to separate the turbulent and non-turbulent regions.

Usually, these measurement techniques are performed with a stationary camera set to measure only a part of the flow. Flow structures travel in and out of the field of view during the measurement. This is problematic for experiments on the long-time behaviour of turbulent structures, and measurements in the co-moving frame can significantly lengthen the observation time.

To analyse the interaction between the turbulent and non-turbulent regions, the exact location of the interface needs to be known at each frame. So, the instantaneous velocity and concentration information are required to analyse the TNTI.

When using a stationary camera system, a large field of view allows a lot of time for the flow structures to be measured, while a small field of view grants a high resolution of the measurement. This forces the experimentalist to choose between the resolution of the measurement or the amount of time an event can be measured. Of course, it would be ideal to have both a lot of time to measure the large-scale structures and high resolution to resolve the small-scale structures.

In an attempt to have both high-resolution measurements and to follow events for as long as possible, this thesis proposes to move the camera system along with the large-scale fluid motion. However, moving the cameras introduces new challenges.

A much larger section of the flow will need to be illuminated compared to a stationary measurement. So, a large distance between the mirrors and measurement location is needed to expand the laser beam into a large sheet. This also increases the need for a powerful laser because the light sheet needs to be bright enough to conduct the LIF measurements while being stretched over a large domain.

As the jet develops downstream, it is entraining fluid and expanding in volume. So, to move along with the interface, the cameras will be mounted to a traverse mechanism set to move in two directions. Chapter 2 will go into detail about the system creating the jet, the illumination setup, and camera movement. As well as some more information about the measurement techniques. At the end, the performance of the setup is tested. The first performance tests are done using a visualisation. The second tests involve the use of stationary PIV measurements.

Measurements have been performed for three jet Reynolds numbers. Each requires different settings for the camera movement and image acquisition software. Chapter 3 explains the different tests that will be performed in addition to more details about each test case's imaging and movement settings. It also contains information on the processing of the PIV and LIF data. The PIV data had to be processed using an in-house MATLAB tool called PIVWare because the software from LaVision could not resolve the large variation in particle displacement in the camera's field of view.

Chapter 4 shows the PIV, edge detection, and conditional vorticity results obtained by processing one of the experiments. In Chapter 5 conclusions are drawn from the results and recommendation for further improvements to this experiment are explained.

2

Experimental Design

To accomplish the goal set in Chapter 1, two measurement techniques are used: particle image velocimetry (PIV) and laser-induced fluorescence (LIF). First, the jet parameters are explained. Next, the design of the experimental setup is discussed. Finally, the performance of the setup is investigated.

2.1. Jet parameters

To nondimensionalize the positions and velocities from the moving measurement, the jet half-width and centreline velocities are required. However, throughout the moving measurements, the centreline of the jet is not in view. Therefore, it is not possible it extract the centreline velocity and jet half-width from these measurements. So, in addition to the moving measurements, a stationary measurement is performed for each Reynolds number. These measurements will be done close to the nozzle to capture the entire jet without the need to make changes to the camera system.

The problem with this approach is that the centreline velocity and jet half-width are only measured in a small part of the test section and cannot be used for the rest of the measurement domain. However, these measurements provide enough information to calculate the centreline velocity and jet half-width for the entire jet by extracting the spreading rate, virtual origin, and decay constant. Figure 2.1 shows a schematic overview of the self-similar jet.

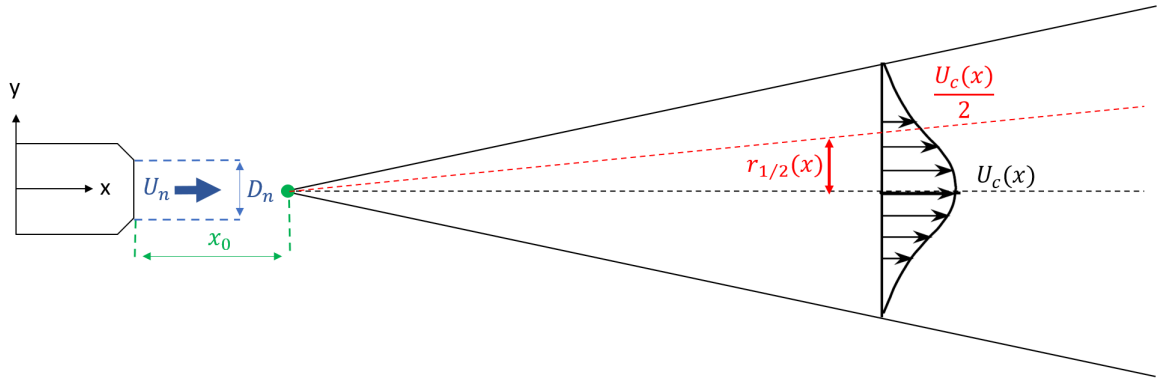

Figure 2.1: A schematic overview of the self-similar jet and the jet parameters.

For a self-similar jet, the jet half-width and centreline velocity can be modeled using Equation 2.1 and Equation 2.2, respectively.

$$r_{1/2}(x) = \frac{d}{dx} r_{1/2} \cdot (x - x_0) \tag{2.1}$$

In Equation 2.1, $r_{1/2}(x)$ is the jet half-width, a distance x away from the nozzle, $\frac{d}{dx} r_{1/2}$ is the spreading rate and x_0 is the virtual origin of the self-similar region. The spreading rate is the slope of the

dashed red line in Figure 2.1.

$$U_c(x) = \frac{B_u D_n U_n}{x - x_0} \tag{2.2}$$

Equation 2.2 gives the relation between centreline velocity and distance from the nozzle. In this equation, $U_c(x)$ is the centreline velocity at distance x from the nozzle, D_n is the nozzle diameter, U_n is the nozzle exit velocity, x_0 is again the virtual origin and B_u is the decay constant [1, 5].

To obtain the jet parameters, a simple linear fit can be performed on the averaged velocity data from the stationary measurements. Table 2.1 shows an overview of these parameters as found in literature.

Source	Re	Spreading rate $\frac{d}{dx} r_{1/2}$	Virtual origin x_0/D_n	Decay constant B_u
Case 5 from Ref. [6]	1.2×10^4	0.082	1.1	5.6
Ref. [7]	2.0×10^3	0.096	6.8	6.7
Ref. [5]	2.4×10^3	0.093	4.9	5.9
Ref. [8]	$\sim 10^5$	0.094	4.0	5.8
Ref. [9]	1.1×10^4	0.096	-	6.1
Ref. [10]	8.7×10^4	0.086	-	5.9
Ref. [11]	$\sim 10^5$	0.086	3	5.7

Table 2.1: An overview of the spreading rate, virtual origin, and decay constant as found in the literature. This table is adopted from Ref. [6]

2.2. Final experimental design

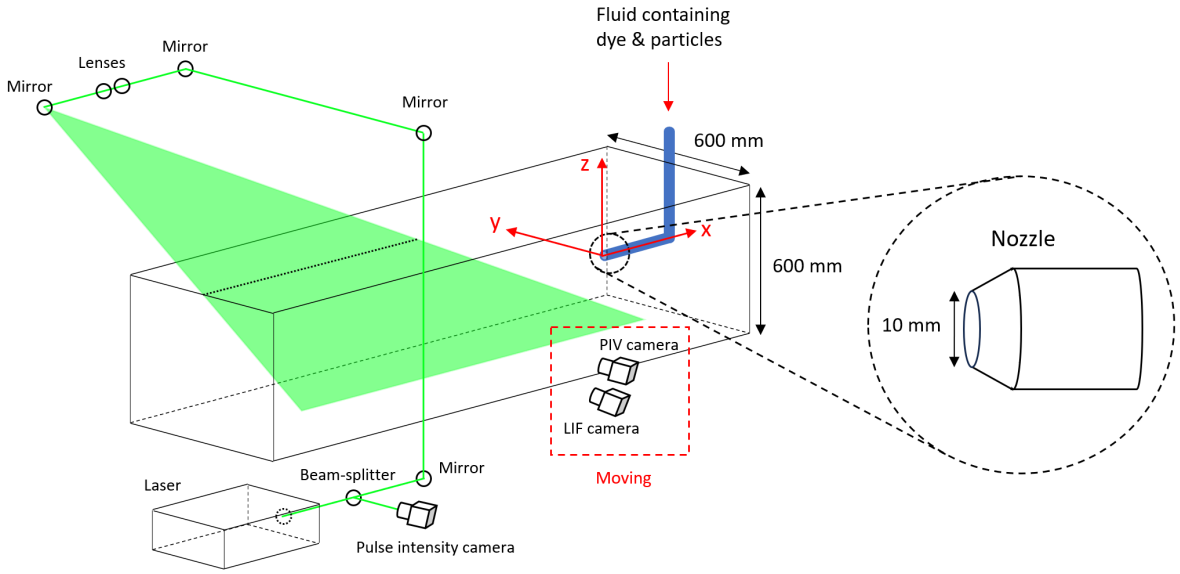

Figure 2.2: Schematic view of the experimental setup. The laser sheet is directed to the middle of the water channel by a set of mirrors and made into a sheet by lenses.

Measurement techniques

For this experiment, two measurement techniques will be used. These are Particle Image Velocimetry (PIV) and Laser Induced Fluorescence (LIF).

PIV is used to measure the fluid velocity. The fluid is seeded with Spherical® hollow spherical glass particles. These particles have a nominal diameter of $11.7\ [\mu m]$ and a density of $1.1\ [g/ml]$. These particles are imaged in two different instances. The particle displacement between images and exposure time delay are used to calculate the instantaneous fluid motion.

LIF is used to measure dye concentration. A fluorescent dye is added to the flow and illuminated by laser light. The dye absorbs and emits light at different wavelengths. The intensity of the emitted light depends on the intensity of the light source and the concentration of dye. So, for a light source with a constant light intensity, the intensity of the emitted light depends only on the dye concentration. Converting the emitted light intensity back into concentration requires calibration.

Calibration is performed by positioning a tank in the measurement domain and filling it with a solution of water and dye for which the concentration is known. This process is repeated until an increase in dye concentration no longer results in an increase in light intensity. The aim of the calibration procedure is to determine the proportionality constant between the dye concentration and fluorescence intensity.

For this experiment, LIF will be used to distinguish between the jet and outside regions. For this specific use case, the dye must have a high Schmidt number. So, the molecular diffusion rate is low compared to the viscous diffusion rate, and the dye will largely remain in the turbulent jet. This large difference in dye concentration between the outside and jet fluid results in a large difference in image intensity when this fluid is illuminated. The large difference in image intensity will be used to find the position of the TNTI. The dye used for this experiment is Rhodamine 6G, which has a Schmidt number approximately equal to 2.9×10^3 [12].

Creating the jet

The device making the turbulent jet is largely the same as described in the master thesis of Lyke van Dalen [6], except that it has been adjusted to perform measurements in the water tunnel. The test section is $5\ [m]$ long and has a cross-sectional area of $600 \times 600\ [mm^2]$. It has two advantages compared to the setup of Ref. [6]. First, the larger volume of water should make the LIF measurements easier because the background concentration of dye increases at a slower rate. This makes it possible to do more measurements before the water has to be replaced or cleaned. Second, the absence of a

back wall ensures that the region of interest is not affected by backflow, removing one of the temporal constraints in Ref. [6].

The jet flow is supplied by a centrifugal pump (SAER 32/2), connected to a reservoir containing $60\,[L]$ of water. Before the water leaves the nozzle, it passes through one of two available flow meters. The two flow meters are for a different range in flow rate. These are the B.I.O.-Tech FCH-midi-POM which is used for flowrates between $0.1[L/min]$ and $10[L/min]$ and the Badger 3012 4F16 for flowrates between $5\,[L/min]$ and $65\,[L/min]$. These have an accuracy of 2% and 3%, respectively. The flow meter data is recorded using LabVIEW on a separate computer.

The reservoir is filled with water from the water tunnel, which has been seeded with PIV particles by hand. This is done to ensure the particle concentration of the jet and background is the same. The fluorescent dye is added to the reservoir next. The dye is mixed in the reservoir using the recirculation feature of the setup before the experiment [6].

Illumination

The particles and dye are illuminated using a Spectra-Physics Quanta Ray double pulse Nd:YAG laser. This laser emits green light at 532 nm and has a repetition rate of $15\,[Hz]$. The laser beam is directed upward towards a set of mirrors and lenses mounted above the water tunnel as shown in Figure 2.2. The lenses turn the laser beam into a thin sheet of laser light projected into the flow. However, the laser sheet has to pass through the water surface first. To prevent the light sheet from moving due to movement in the free surface of the water, a small PMMA box is placed in the water. The light sheet passes through the PMMA box instead of the free surface and will not be disturbed by its movement. The light sheet is positioned in the centre of the jet and does not move during the experiment.

For the LIF measurements, it is assumed the light intensity of the source is constant. However, pulsed lasers can have slight differences in energy output between pulses. This is referred to as the pulse-to-pulse variance of the laser. This setup includes an extra camera that measures the pulse intensity. These measurements could be used to investigate the pulse-to-pulse variance of the laser and correct it in the LIF measurements. So, before the laser beam hits the first mirror, it passes through a beam splitter that directs part of the laser beam to this additional camera.

Camera Movement

LaVision Imager sCMOS CLHS cameras are used for the PIV and LIF measurements and are mounted to a traverse mechanism that allows movement in three directions. The traverse mechanism consists of large aluminium axes driven by MDrive 23 Hybrid step motors. The x-axis is 2 meters long and is set parallel to the jet. The y and z axes are both 1 meter long. The traverse mechanism is controlled using LabVIEW on the same computer reading the flow meter signals.

The PIV and LIF cameras are about 10 cm apart. The PIV camera is pointed straight at the jet, and the LIF camera is at a slight angle to align the field of view of both cameras. Both cameras are fitted with light filters to ensure that the PIV camera records only the light scattered by the PIV particles and the LIF records only the light emitted by the fluorescent dye.

The camera measuring the laser pulse intensity is a LaVision Imager intense and is mounted on a tripod next to the laser. The specifications for these cameras can be found in Table 2.2.

Camera	Purpose	Sensor type	sensor size [mm]	pixel size $[\mu m]$	resolution
1	LIF	sCMOS	16.6 x 14.0	6.5 x 6.5	2560 x 2160
2	PIV	sCMOS	16.6 x 14.0	6.5 x 6.5	2560 x 2160
3	Pulse intensity	CCD	16.93 x 16.93	6.45 x 6.45	1376 x 1040

Table 2.2: Specifications for each camera.

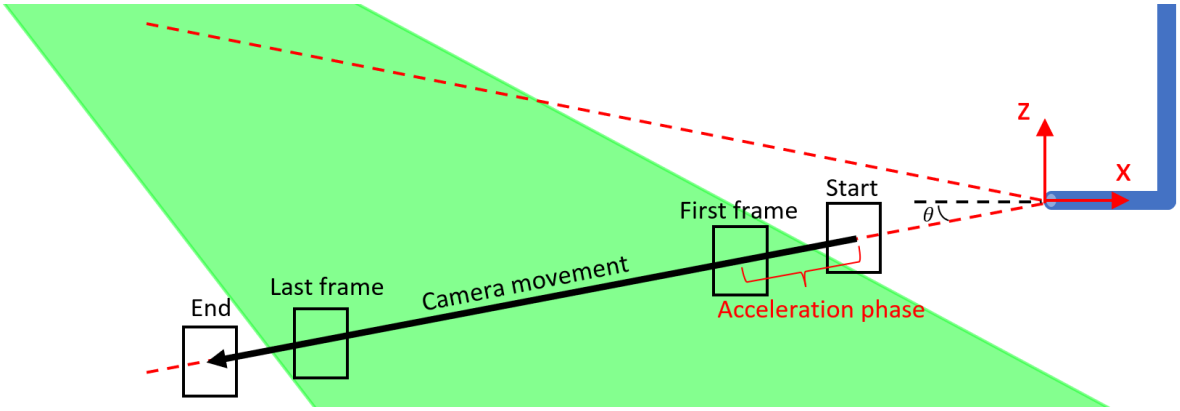

Figure 2.3: Schematic view of the camera movement. The red lines indicate the expected location of the jet edge. "Start" and "End" indicate the start and end positions of the camera movement throughout a measurement. "First frame" and "Last frame" refer to the first and last fully illuminated frame. θ is the angle of the camera movement.

The camera movement is shown in Figure 2.3. Depending on the test case, the movement starts partly in the illumination shadow or at the nozzle. Higher Reynolds numbers require a higher camera velocity. So, the cameras need more space to accelerate. The images recorded during the acceleration phase of the cameras will not be used due to inconsistent trigger rates. The starting position is chosen to make sure the FOV is fully illuminated once the cameras travel at constant velocity.

Laser timing

The traverse mechanism triggers the laser and camera systems. This is shown schematically in Figure 2.4. The trigger from the traverse mechanism is received by the Programmable Timing Unit (PTU). The PTU triggers the cameras to record a frame and triggers the laser cavities to illuminate the cameras. The laser cavities receive two separate triggers. The first triggers the flash lamps of the laser cavity to illuminate the Nd:YAG crystal. This starts the build-up of energy within the laser cavity [13]. The second trigger goes to the Q-switch. When the Q-switch is activated, the energy withing the laser cavity is released in the form of a short light pulse [13]. The PIV and LIF cameras are configured to record images in pairs of two to decrease the particle displacement. The time difference Δt between images A and B is the exposure time delay. The time between image pairs for this laser is $66.7\ [ms]$. The cameras mounted to the traverse mechanism will have moved a distance Δx downstream between image pairs. The laser intensity camera operates in single-frame mode and records only the intensity of the first laser pulse.

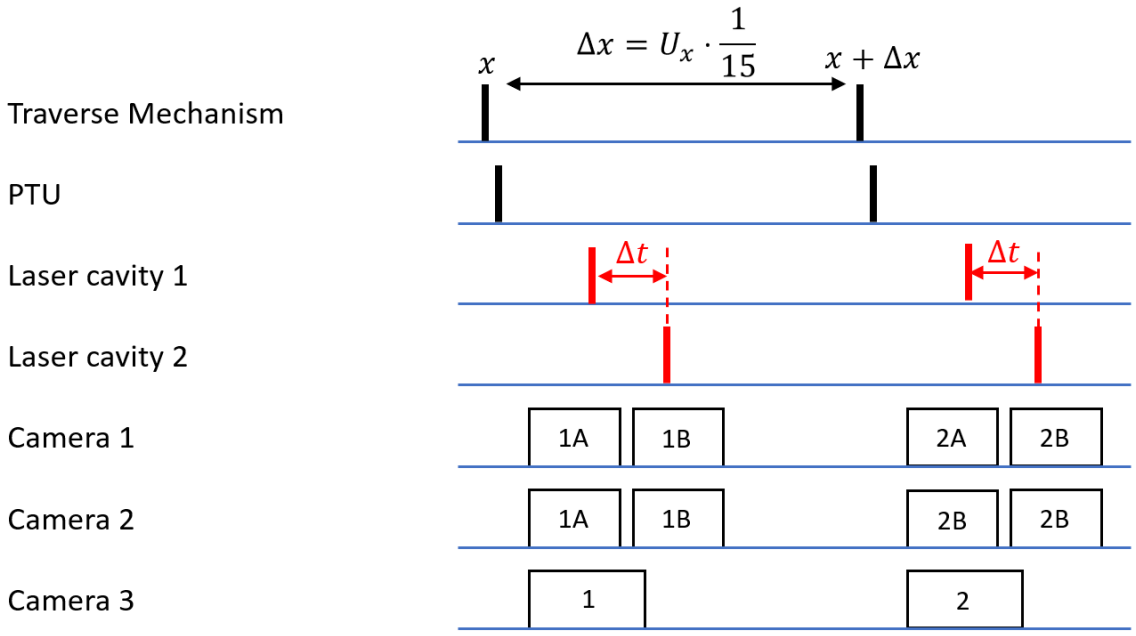

Figure 2.4: Timing diagram of the setup.

2.3. Performance of the setup

Two tests have been performed to ensure that the setup was working as intended. The first test is a visualisation. This visualisation is performed to determine if the device creating the jet is still working as it was in Ref. [6].

Visualisation

To visualise the jet, methyl blue dye is added to the reservoir, and the jet is recorded using a GoPro Hero 7 camera. The red images of the recording are extracted and averaged to get the image shown in Figure 2.5. The red signal was extracted because it gave the best contrast between the background and the jet. For this visualisation, a nozzle with a diameter of $5\,[mm]$ was used, and the Reynolds number is approximately 2.7×10^4. For this quick analysis, it is assumed the dye concentration represents the jet's velocities.

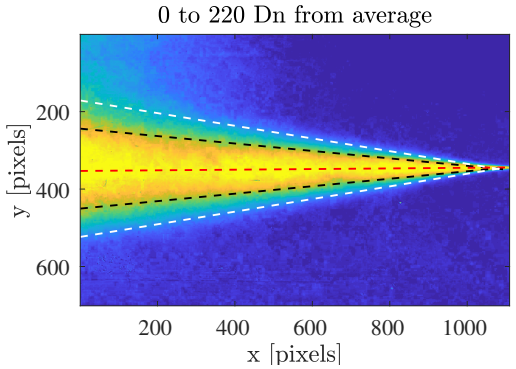

Figure 2.5: 0 to 220 times the nozzle diameter of the visualisation with the centreline in red, the half-width in black, and the edge in white.

The highest image intensity is identified as the jet centreline, and half of this intensity is marked as the half-with. This gave an approximate spreading rate of 0.096 and a virtual origin between $2D_n$ and $18D_n$. Comparing these values with the data from Table 2.1, it was concluded that the jet device was performing as expected.

Jet alignment

With the jet device functioning as intended, the structure for the light sheet was built, and the laser and camera movement systems were installed to start measuring the jet using PIV. The jet was measured using stationary PIV at eleven different positions. These measurements were averaged and assembled to get the complete averaged jet. This result can be seen in Figure 2.6. Initially, these measurements were intended to characterise the jet and nondimensionalize the results from the moving experiments. However, processing these measurements resulted in very odd values for the jet characteristics. Moreover, the self-similar velocity profiles deviated from those in Ref. [4]. This was most apparent in the self-similar profile of the streamwise velocity fluctuations. Ref. [4] shows that the profile for velocity fluctuations in streamwise direction has two peaks that are slightly off centre as shown in Figure 4.2. This distinct double peak could not be found in the profile from the current measurement. It was found that these odd characteristic values and mismatched velocity profiles were due to a misalignment in the nozzle. So, before continuing with the moving measurements, the jet was properly aligned to the centre of the water tunnel. None of the measurements before realignment of the nozzle have been used for the rest of this research.

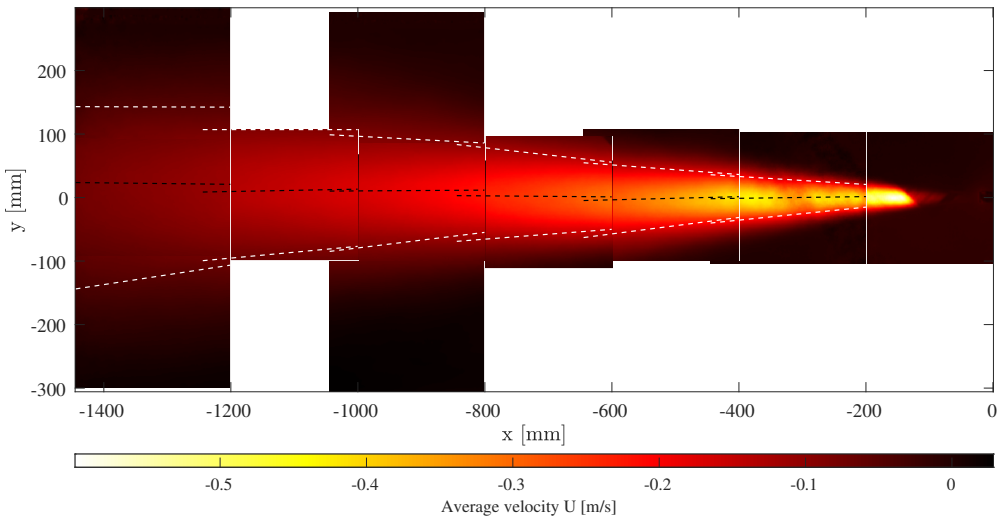

Figure 2.6: Reconstruction of the eleven measurements at $Re \approx 3.1 \times 10^4$. It shows the jet from approximately $11D_n$ to $145D_n$ in x and from $-30D_n$ to $30D_n$ in y. The black line is the centreline, and the white lines indicate the half-width. The color relates to the magnitude of average velocity U in $[m/s]$. The sudden jump in velocity in the rightmost image is where the jet enters the light sheet.

3

Test plan & Processing

3.1. Test plan

Choice of Reynolds numbers

Three Reynolds numbers will be tested. These are approximately 9×10^3, 1.2×10^4 & 3.1×10^4. $Re \approx 1.2 \times 10^4$ made an excellent starting point because it is the only Reynolds number tried in Ref. [6]. Initially, the intention was to test Reynolds numbers lower than 9×10^3 to get a larger range in Reynolds numbers. However, because of memory constraints, adding the laser profile camera and the double frame LIF measurement reduced the number of frames that the acquisition computer could record. With the fixed repetition rate of $15\,[Hz]$ for this laser, a decrease in the total amount of frames results in less recording time. Therefore, either the velocity of the camera had to be increased, or the measurement domain had to be decreased. The camera velocity has been estimated in Ref. [6] to cover a range of velocities found in the measurement domain and this velocity was linearly scaled to fit the other Reynolds number. So, the increase in camera velocity also requires an increase in Reynolds number. Because great effort had been made to make the measurement domain as large as possible, the choice was made to increase the Reynolds number as opposed to measuring a smaller part of the the flow. $Re \approx 3.1 \times 10^4$ was chosen because it is the highest Reynolds number that could be achieved with the experimental setup.

Camera & movement configuration

For the first 30 experiments, the starting position is not defined by the movement mechanism. Instead, the first frame of each recording has the nozzle in view. The location of the nozzle tip is defined as $X = 0$ for all experiments. So, the location of the camera during these measurements can be derived from this first recorded frame, and the starting position of these experiments is marked as "From recording" in both Table 3.3 and the experiment log. The camera movement of these experiments is shown schematically in Figure 3.1. This change of starting position and trigger setup was made between experiments because of the desire to add double frame LIF measurements. The new camera movement is shown schematically in Figure 3.2. For the measurements with $Re \approx 1.2 \times 10^4$ and $Re \approx 3.1 \times 10^4$, the amount of frames has been changed partway through the experiment. For $Re \approx 1.2 \times 10^4$, this was done to accommodate the addition of the double frame LIF. For $Re \approx 3.1 \times 10^4$, the starting position was moved closer to the nozzle, subsequently increasing the total amount of frames, to give the laser more time to warm up.

For the experiments with a predefined starting position, the acceleration of the cameras is partly inside the illuminated area. However, these frames are not used because the illumination shadow is still in view and the laser cavity is still increasing in temperature (see section 3.3).

The FOV centre starting position is $32D_n$ away from the tip of the nozzle. This is to ensure that the flow is self-similar in the measurement domain. The size of the FOV size was also taken from Ref. [6]. The proof of concept measurement showed that this FOV approximately captures engulfment events throughout the experiment. The consequence of a static FOV in this experiment is that the FOV is larger than necessary for the beginning of the measurements and slightly too small for the end of the measurements.

The angle for the camera movement deviates from the one found in Ref. [6] and what is expected from the spreading rate of the jet. When trying an angle of 11°, it was found that the cameras moved too far from the jet at the beginning of the experiment. Therefore, the angle was slightly lowered to be better in line with the angle of the jet edge. The details for the camera movement, lens, and image acquisition software configuration can be found in Table 3.1, Table 3.2 and Table 3.3, respectively.

Re	X_{FOV}/D_n [-]	Y_{FOV}/D_n [-]	θ [°]	$U_x\ [cm/s]$	$U_y\ [cm/s]$	$a_x\ [cm/s^2]$	$a_y\ [cm/s^2]$
9×10^3	$32 - 80$	$4.78 - 11.96$	8.5	1.5	0.22	1.5	0.22
1.2×10^4	$32 - 80$	$5.07 - 12.67$	9.0	2.0	0.32	2.0	0.32
3.1×10^4	$32 - 80$	$5.07 - 12.67$	9.0	5.2	0.82	5.2	0.82

Table 3.1: Parameters for the moving tests. X_{FOV} and Y_{FOV} are the range of positions of the centre of the FOV expressed in nozzle diameters (D_n). These positions are relative to the tip of the nozzle. The experiment starts close to the nozzle. U_x/U_y and a_x/a_y are the velocity and acceleration of the cameras, respectively. The velocity is set to approximately follow the large engulfment eddies of the jet. The cameras accelerate in one second to the desired velocity.

Camera	Purpose	FOV [mm]	M_0	f-stop
1	PIV	105.5 x 127.7	0.13	5.6
2	LIF	105.5 x 127.7	0.13	4.0
3	Pulse intensity	No lens		

Table 3.2: Specification of the camera system. The magnification follows from the choice of FOV and the camera sensor size. The f-stop of the LIF camera was lowered compared to the PIV camera to let in more light. The camera measuring the laser pulse intensity was not fitted with a lens. Hence, the lack of FOV, magnification and f-stop settings.

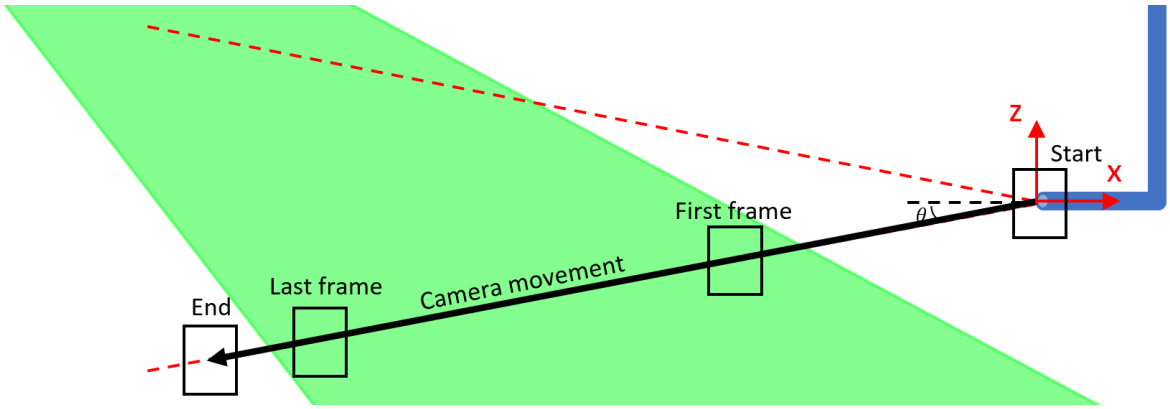

Figure 3.1: When the starting position is marked as "From recording", the camera movement starts from the nozzle before the measurement is started. Therefore, the precise location of the cameras will need to be extracted from the recording.

Re	$\frac{X_{start}}{D_n}$	# Frames	$\Delta t\ [ms]$	$E_m\ C1$	Number of repetitions
9×10^3	29	504	5	double	40
1.2×10^4	"From recording"	580	4	single	26
1.2×10^4	28	400	4	double	16
3.1×10^4	20	175	2	double	10
3.1×10^4	0	200	2	double	51

Table 3.3: This table summarizes all the settings of the Davis acquisition program for the different Reynolds numbers. $Re \approx 1.2 \times 10^4$ and $Re \approx 3.1 \times 10^4$ are split in two due to the difference in starting position and amount of frames. The distance between the centre of the FOV and the tip of the nozzle is expressed in nozzle diameters and denoted with X_{start}/D_n. The exposure time delay and exposure mode are denoted with Δt and E_m, respectively. $C1$ indicates cameras 1. Cameras 2 and 3 are set to double frame and single frame, respectively.

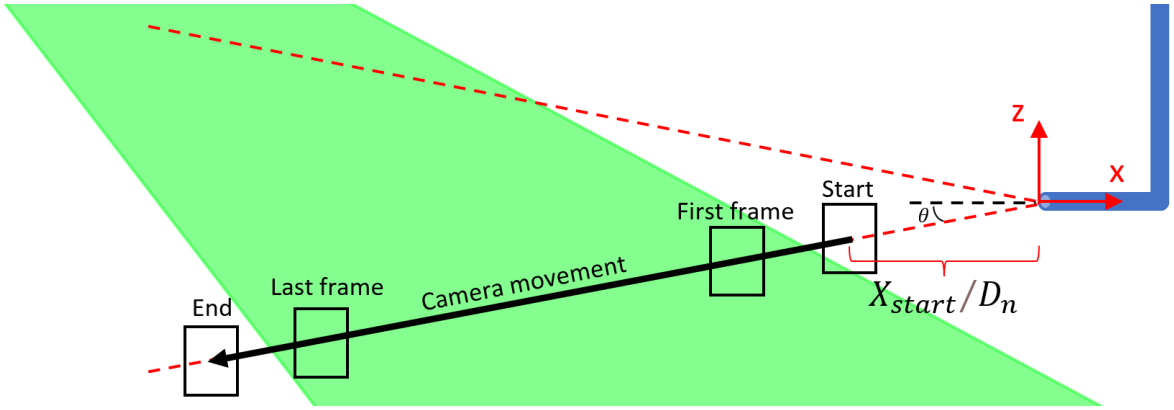

Figure 3.2: When the starting position is predefined, the cameras are moved to the starting position X_{start}/D_n before the measurement. The measurement starts when the cameras start moving from their new starting position.

Changing scales

The biggest challenge of this experiment is the changing of scales during the measurement. The fluid velocity decreases while moving the cameras away from the nozzle, and both the jet half-width and Kolmogorov length scale increase. This affects the particle displacement and spatial resolution during the measurement. The Kolmogorov length scale is estimated using, [1]

$$\eta = \left(\frac{\nu^3}{\epsilon}\right)^{\frac{1}{4}}, \tag{3.1}$$

which requires an estimate of the dissipation rate using, [9]

$$\epsilon = \frac{0.015 U_c^3}{r_{1/2}}. \tag{3.2}$$

The jet characteristics from the stationary measurement were used to extrapolate the jet half-width and centreline velocity for the entire measurement domain.

Figure 3.3 shows an estimation of the Kolmogorov length scale in millimeters and the spatial resolution as a multiple of the Kolmogorov length scale. To fully resolve the flow, the spatial resolution must not exceed 5η according to Ref. [4]. Figure 3.3b shows that this requirement is not met for any of the test cases when considering the smallest interrogation window size in Table 3.4.

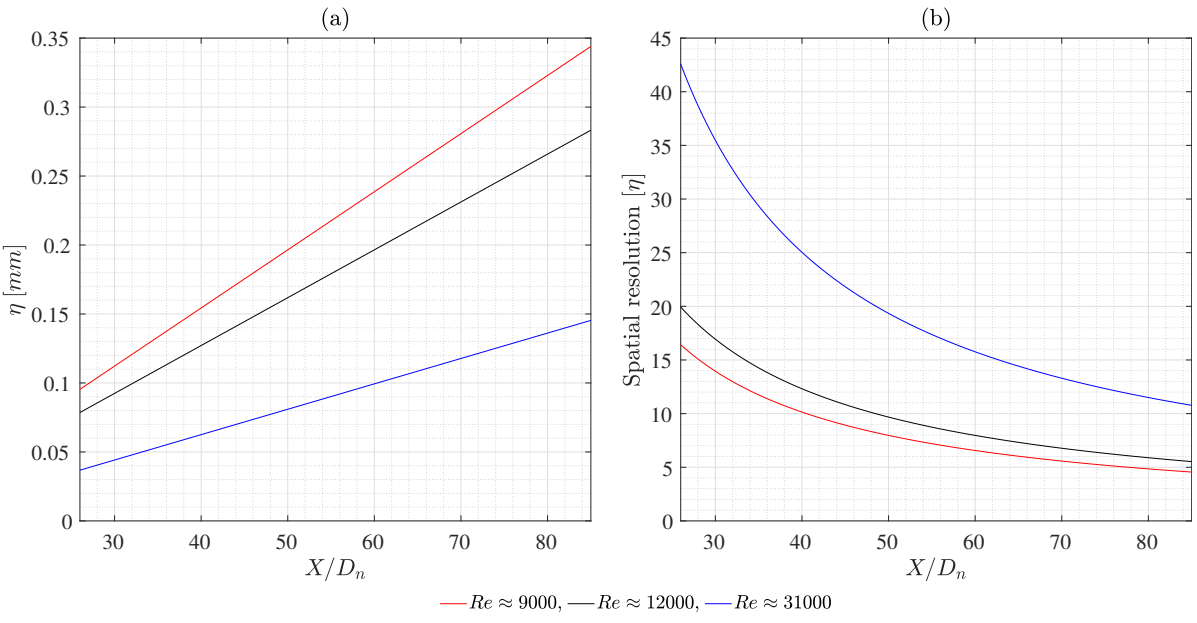

Figure 3.3: a) The Kolmogorov length scale as a function of the downstream position. x/D_n is the distance from the nozzle expressed in nozzle diameters and η is the Kolmogorov length scale in $[mm]$. **b)** The spatial resolution expressed in Kolmogorov length scales as a function of downstream position. The Kolmogorov length is estimated using the centreline velocity and jet half-width from the stationary measurements.

A design rule for any PIV measurement is to limit the pixel displacement to one-quarter of the desired interrogation window size. This is done to limit the loss of correlation because of in-plane displacement. Normally, these displacements are controlled by choosing the appropriate exposure time delay based on the maximum fluid velocity found in the experiment. However, the maximum velocities change during this experiment. Ideally, a laser with a variable exposure time delay is used to keep the particle displacement constant. For this purpose, a diode-pumped Nd:YLF laser has been tried. However, preliminary results with this laser showed that the pulse energy was too low to get images with sufficient exposure of the LIF camera. Therefore, the decision was made to use the laser described in section 2.2, which has a constant exposure time delay, and set it to a value deemed appropriate for most of the experiment. The exposure time delay was also taken from Ref. [6] and the proof of concept measurement showed that resulting the particle displacements can be processed. The exposure time delay for the other Reynolds numbers was adjusted to achieve the same approximate particle displacements of 22 pixels. The constant exposure time delay will result in large particle displacements for the beginning of the measurement and small particle displacements at the end. The largest displacement is found in the first frame of a $Re \approx 1.2 \times 10^4$ experiment is around 36 pixels. At frame 300, the largest particle displacement found is approximately 8 pixels. However, if the typical displacement close to the TNTI is considered, the one-quarter rule is already satisfied at frame 100. It was found that the typical displacement around the TNTI is approximately 5-6 pixels.

3.2. Flow meter measurement

Figures 3.4 and 3.5 show the flow meter measurement during the stationary and moving measurements, respectively. For both figures, the measured data is displayed in blue. The red horizontal lines indicate the target jet Reynolds number proposed in section 3.1 and the subsequent flow rates. During the stationary measurement, the average volumetric flow rate equals $5.88 \pm 0.03\,[L/min]$. For the moving measurement, the average volumetric flow rate equals $5.91 \pm 0.13\,[L/min]$. The flow rate of the stationary measurement was measured using the B.I.O.-Tech flow meter. The flow rate of the moving measurement was measured using the Badger flow meter. The flow rate is converted to a Reynolds number using,

$$Re = \frac{4}{6 \cdot 10^4} \frac{q}{\pi D_n \nu}, \tag{3.3}$$

where q is the flow rate in $[L/min]$, D_n is the nozzle diameter in $[m]$ and ν is the kinematic viscosity in $[m^2/s]$. For these calculations, the kinematic viscosity is assumed to be $1 \times 10^{-6} [m^s/s]$. This results in average jet Reynolds numbers of $1.25 \pm 0.01 \times 10^4$ and $1.25 \pm 0.03 \times 10^4$ for the stationary and moving measurements, respectively.

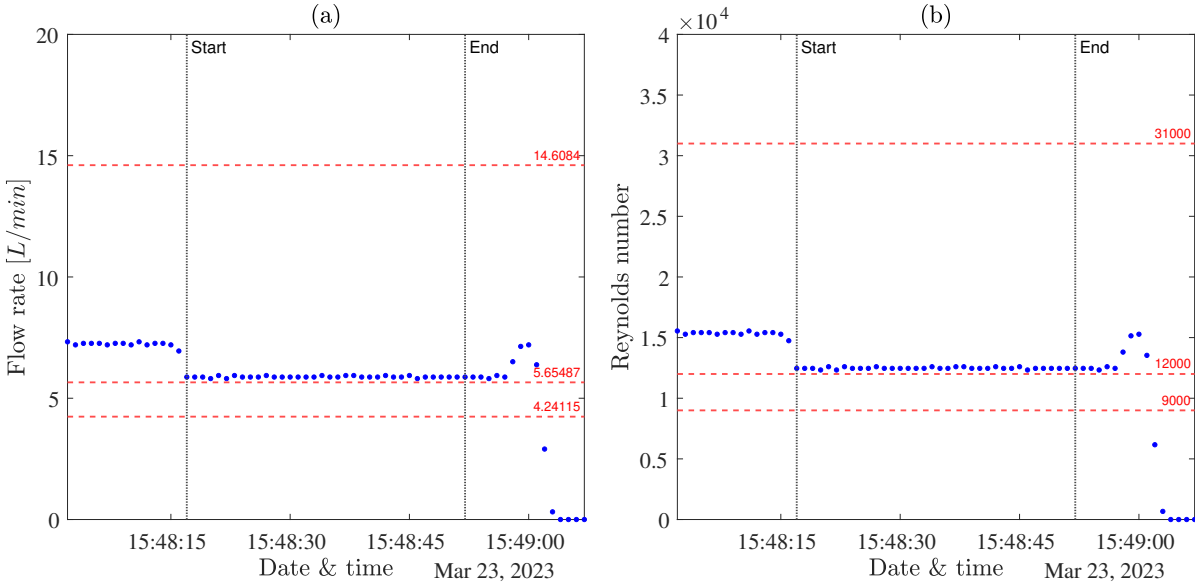

Figure 3.4: a) The volumetric flow rate measurement during the stationary measurement in $[L/min]$. **b)** The resulting jet Reynolds number is calculated from this flow rate. The measurement starts at 15:48:17 and ends at 15:48:57. The horizontal red lines indicate the target flow rates and Reynolds numbers.

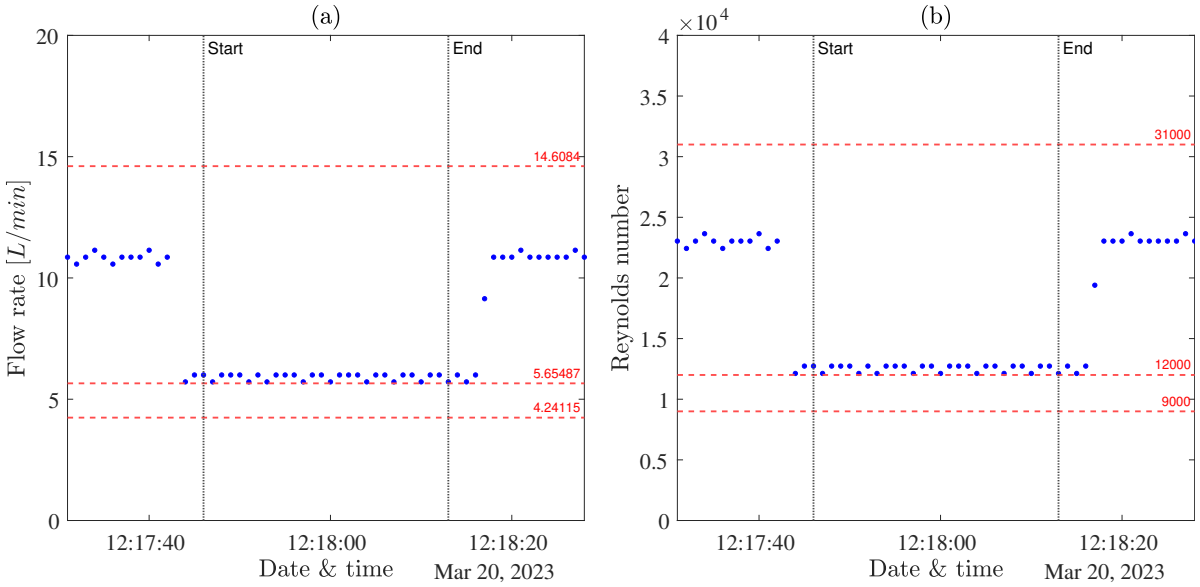

Figure 3.5: a) The volumetric flow rate measurement in $[L/min]$ during the moving experiment. **b)** The resulting jet Reynolds number is calculated from this flow rate. The measurement starts at 12:17:46 and ends at 12:18:13. The horizontal red lines indicate the target flow rates and Reynolds numbers.

3.3. Laser intensity measurement

Figure 3.6 compares the laser intensity measurement to a background measurement of the LIF camera. A background measurement measures the dye concentration that accumulates in the water tunnel. These measurements follow the same path as the moving experiments and are performed to correct the moving LIF measurements for the increasing background intensity. The background measurements are performed without the jet.

The mean intensity of each frame from both cameras is computed from the beginning to the end of the experiment. Initially, the LIF signal sees a decrease. This happens because the nozzle leaves the FOV. The nozzle is made of a clear resin that reflects the laser light well and illuminates the dye in that area. When the laser sheet enters the FOV of the LIF camera, the mean intensity starts to increase again. After frame 200, the illumination shadow is completely out of frame. From this point, the signals are compared. After frame 250, the mean intensity starts to drop again. This can attributed to the increasing volume of fluid containing dye between the laser source and the camera. This lowers the intensity of the light that can be absorbed by the fluid in the FOV.

The laser intensity camera also shows a repetitive w-pattern, and this same pattern can also be found in the LIF camera. However, the fluctuations in this signal are less than three percent, which is within the specifications of the laser.

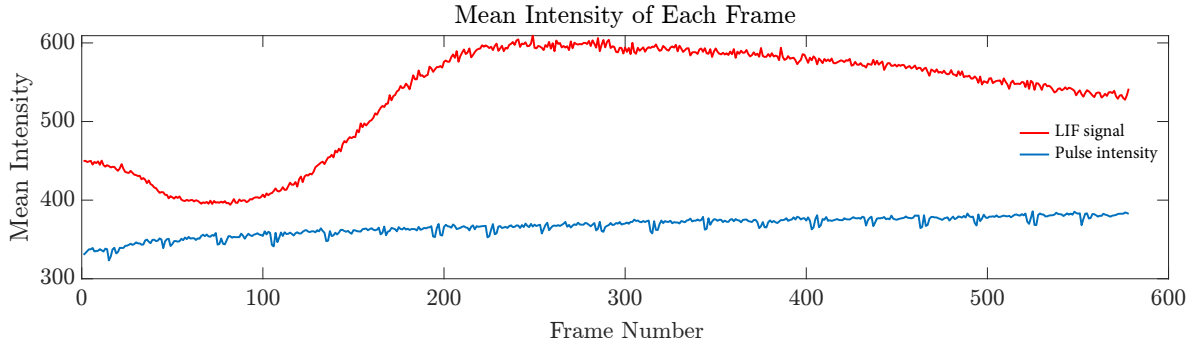

Figure 3.6: The top and bottom figures show the mean intensity and fluctuations, respectively. The intensity fluctuation of a frame is calculated by subtracting the mean intensity of all frames from the mean intensity of that frame. Cam 2 refers to the LIF camera, and Cam 3 refers to the laser intensity camera.

It can also be seen that the laser pulse intensity slowly rises during the measurement. Normally, the flash lamps of the laser keep receiving triggers from the PTU to keep the laser cavity at its operating temperature. However, for this experiment, the camera traverse system only sends the trigger pulses during the forward movement; see Figure 2.4. This creates a problem during the idle time between measurements because the laser is not receiving flash lamp triggers when the camera moves back to the starting position. This has the unintended consequence of lowering the laser cavity temperature, which causes the laser temperature to rise during the measurement slowly. Subsequently increasing the light output. The idle time of the laser should be reduced by also supplying laser triggers during the movement back to the starting position.

3.4. Processing

The methods discussed in the processing section are tested for a single moving measurement. However, the measurements concerning the other Reynolds numbers can be calculated using the same PIVWare configuration because the exposure time delay is adjusted according to the nozzle exit velocity, resulting in approximately the same particle displacement range. The LIF processing is not tailored to one specific Reynolds number and should also be valid for all measurements. The moving measurements that are processed have a Reynolds number $\approx 1.25 \times 10^4$ and a starting position $X_{start}/D_n = 28$. Details on this measurement can be found in Section 3.1.

3.4.1. PIV

PIV interrogation analysis is performed using an in-house tool called PIVware by Jerry Westerweel, which is implemented for use in MathWorks MATLAB. It allows more flexibility than LaVision's Davis regarding interrogation window shape and size. These custom interrogation windows are beneficial when dealing with large pixel displacements due to the fixed exposure time delay and changing velocities.

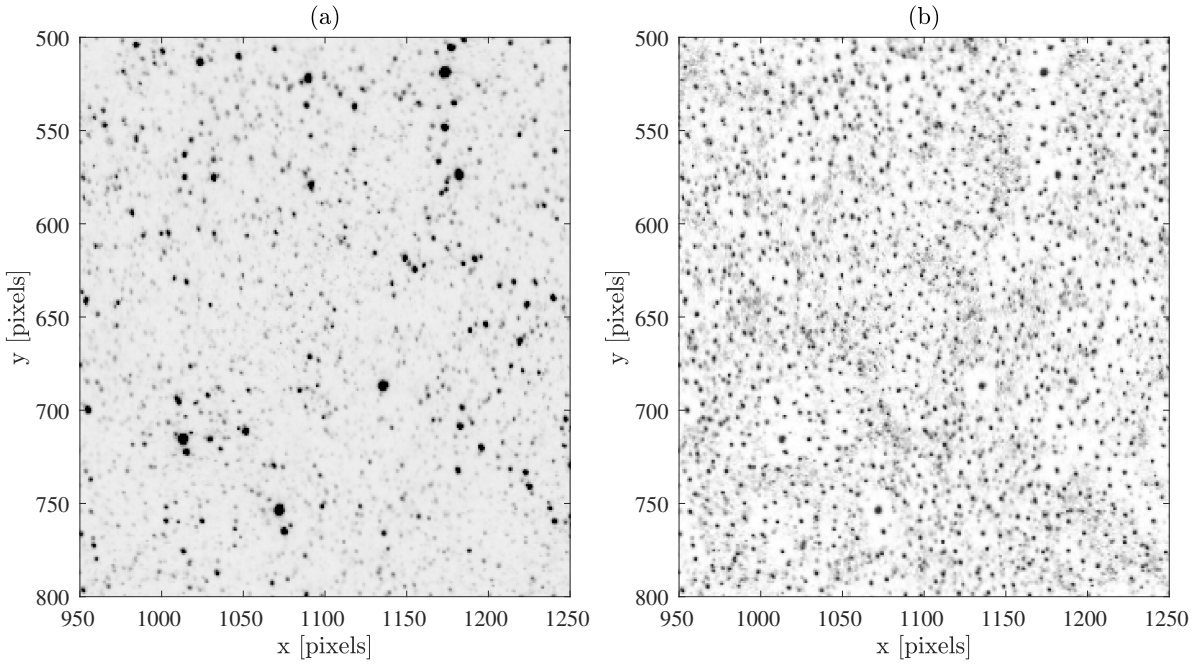

Figure 3.7: Figures **(a)** and **(b)** show frame 150 before and after applying a min-max filter, respectively. The images are zoomed in to better show the effect of the filter.

Min-max filter

The first step in processing is the application of a min-max filter [13]. Figure 3.7 shows frame 150 before and after this filter. It normalizes the local image contrast and reduces the amount of spurious vectors in the final PIV result [13].

The filter length of the min-max filter was tuned to give the best results for this experiment. The optimum filter length is calculated in two steps. First, a range of filter lengths is applied to a range of frames within the experiment. These frames are processed and validated using the methods described later in this section. Next, the mean fraction of spurious vectors is calculated for each filter length. The resulting graph can be found in Figure 3.8. It shows that filter lengths of 4 to 13 pixels give approximately the same average of 1.6% spurious vectors for this experiment. However, all filter lengths greatly improve the result without a min-max filter, which is an average of 6.83% spurious vectors. Filter length 8 gave the best result and was used to process the PIV measurement.

Multigrid PIV

The velocity calculations were done using multigrid interrogation as described in Ref. [13]. Table 3.4 summarizes, in order, all window sizes used. In section 3.1, it was discussed that the in-plane displace-

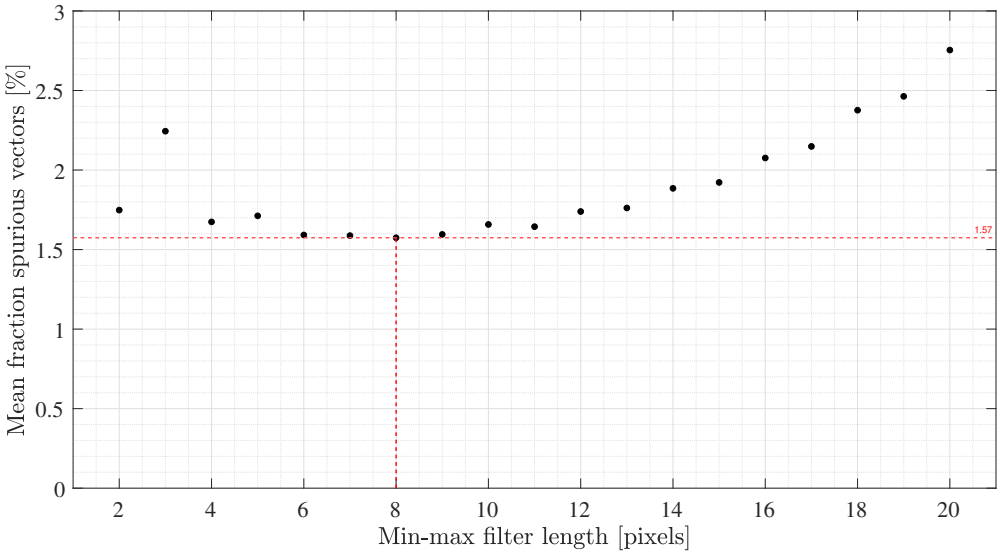

Figure 3.8: For this experiment, the min-max filter length is varied from 2 to 20 for frames 50 to 400 in increments of 10 frames. The mean percentage of bad vectors as a function of filter length is used to show which filter length results in the best PIV result. Filter length 8, marked in red, is chosen for the final calculation. Without a min-max filter, the mean fraction of spurious vectors is equal to **6.83%**.

Order of use	1^{st}	2^{nd}	3^{rd}	4^{th}
Size $[px]$	256×64	128×64	64×32	32×32
Vector spacing $[px]$	128×128	64×64	32×32	16×16

Table 3.4: This table shows the order and size of the interrogation windows sizes used. The window size is displayed in pixels.

ment could be as large as $36\ [px]$. This is more than the entire interrogation window size in the case of commonly used $32 \times 32\ [px]$ interrogation windows; the particles within would certainly be lost. To solve this, the first three interrogation windows are elongated. Increasing the size of the interrogation window in the direction of the largest displacement reduces the amount of particles lost due to in-plane displacement. Compared to large square interrogation windows, the benefit of this is the reduction in computational load for the other direction. Moreover, it improves the estimation of the velocity because the $\partial u/\partial y$ is smaller. Figure 3.9 shows intermediate results for different interrogation window sizes. The results are smoothed between the interrogation steps by replacing the vectors with their median. This median filter acts like a low pass filter and makes the estimate more robust before the next interrogation. The median is calculated using the surrounding vectors in a $5 \times 5\ [px]$ region. After the final interrogation, the total amount of vectors is $(113 \times 145) = 16385$ with 50% overlap.

Next, the spurious vectors are replaced. Spurious vectors are identified using a median test. This step also considers a vector region the size of $5 \times 5\ [px]$. However, the residual is considered instead of replacing the vector with its median. The vectors with a residual equal to or larger than three are replaced by an interpolated vector calculated using the surrounding valid vectors in a $3 \times 3\,[px]$ region. A frame is considered to have a good result if the percentage of spurious vectors is less than five percent [13]. This norm follows from the assumption that a spurious vector must be surrounded by enough valid vectors in order to properly recognize it as a spurious vector and to have enough valid vectors the replace it [13].

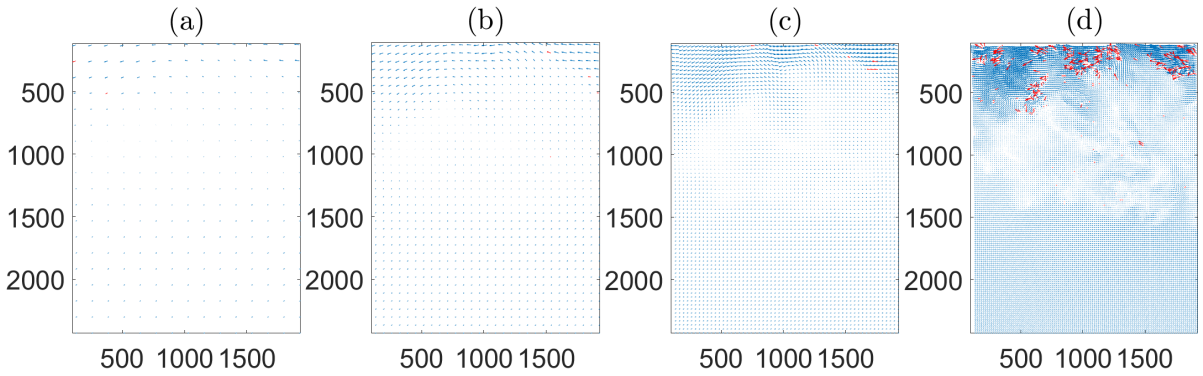

Figure 3.9: The arrow plots **(a)** to **(d)** show the results for the different interrogation window sizes in the same order as found in Table 3.4. The spurious vectors are marked red.

3.4.2. LIF Edge Detection

Automatic edge detection

At first, the TNTI is detected automatically using the same detection method as described in Ref. [6], which is an adaptation of the method proposed in Ref. [15]. The original algorithm works by calculating the average intensity of the image above a threshold as a function of that threshold for each frame. Figure 3.10 shows the curve that results from this process from Ref. [14]. In Ref. [14], two lines tangent to the average intensity curve are identified. These are the red dashed lines in Figure 3.10. The point of intersection of these two dashed lines is taken as the threshold value separating the turbulent and non-turbulent regions for that frame.

The method from Ref. [6] calculates the derivative of the average intensity and defines the threshold of the TNTI at the minimum of this curve. An example of this can be found in Figure 4.8 **(a)**.

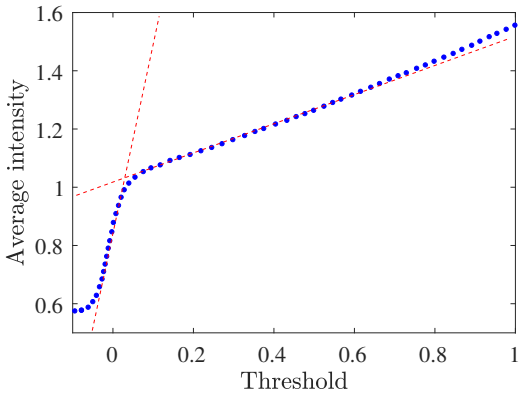

Figure 3.10: Visualisation of the threshold detection from Ref. [14]. "Selection of the detection threshold for the jet fluid using the method of Prasad and Sreenivasan (1989). The dashed lines intersect at a threshold value of 0.03".

It was found during the implementation of this method that there were instances the algorithm could not determine a proper threshold. This was caused by erratic behaviour in the average intensity at high values for the threshold. So, an upper limit of 1300 is imposed on the threshold. Higher values for the limit result in the problem the limit is meant to solve for the first frames of the experiment. Moreover, Figure 3.12 shows that the expected intensity threshold is not above 1000 in this case.

Figure 4.8 shows the behaviour of the automatic edge detection algorithm for two different frames in this measurement. When comparing these frames to Figure 3.10, it can be noticed that there are two inflection points in the average intensity curves instead of a single one. This extra inflection point creates confusion when it comes to choosing the proper intensity threshold. This can be seen in Figure 4.7 **(a)**, where both local minima correspond to a jump in the intensity field. During processing of the LIF measurement, it was found this method does not consistently produce the outermost interface of the jet. This is further explained in subsection 4.2.2. Therefore, another way of finding this interface is needed.

Manual edge detection

Because only one experiment was analysed for the purpose of writing this thesis, the choice was made to go through a set of every 15^{th} frame of the measurement and choose an appropriate intensity threshold that makes visual sense. This is illustrated in Figure 3.11, where it becomes clear that figure **(b)** shows an intensity threshold that is most appropriate for this frame. The lower intensity threshold, depicted in figure **(a)**, draws the edge too far into the outside of the jet. On the other hand, the higher intensity threshold, depicted in figure **(c)**, draws the edge too far into the jet. Through these data points, a fourth-order polynomial was fitted to get a function that gives the threshold value for each individual frame in the measurement. Table 3.5 compares the root-mean-square error (RMSE) and R^2 values of third-, fourth-, and fifth-order polynomials. The fourth-order polynomial is chosen because it has the lowest RMSE of the three. Figure 3.12 shows the result of this process. However, doing the edge detection this way is not an option for the remainder of the measurements. One possibility would be to calculate the threshold value, using the automatic method, for a specific location across all measurements of the same Reynolds number. And use the average of these values instead of the value for the individual measurement to determine the interface. This may remove the sudden peaks seen in Figure 3.12.

Order	3^{rd}	4^{th}	5^{th}
$RMSE$	50.7	45.5	46.2
R^2	0.87	0.90	0.90

Table 3.5: The $RMSE$ and R^2 values that result from fitting the different order polynomials to the selected threshold values seen in Figure 3.12.

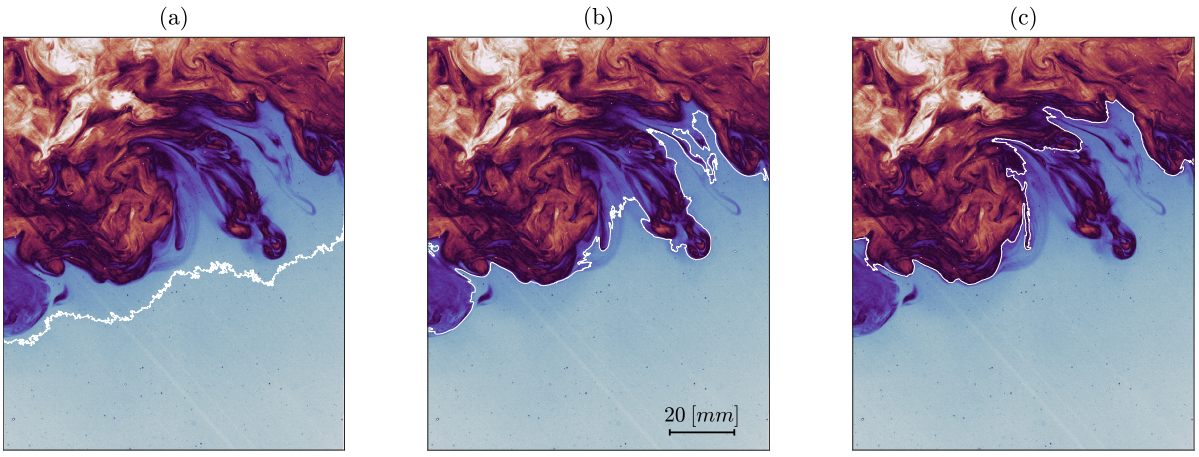

Figure 3.11: This figure depicts the raw LIF image from frame 225 with the proposed TNTI drawn in white based on the different intensity thresholds. **a)** Intensity threshold $= 700$. **b)** Intensity threshold $= 900$. **c)** Intensity threshold $= 1100$.

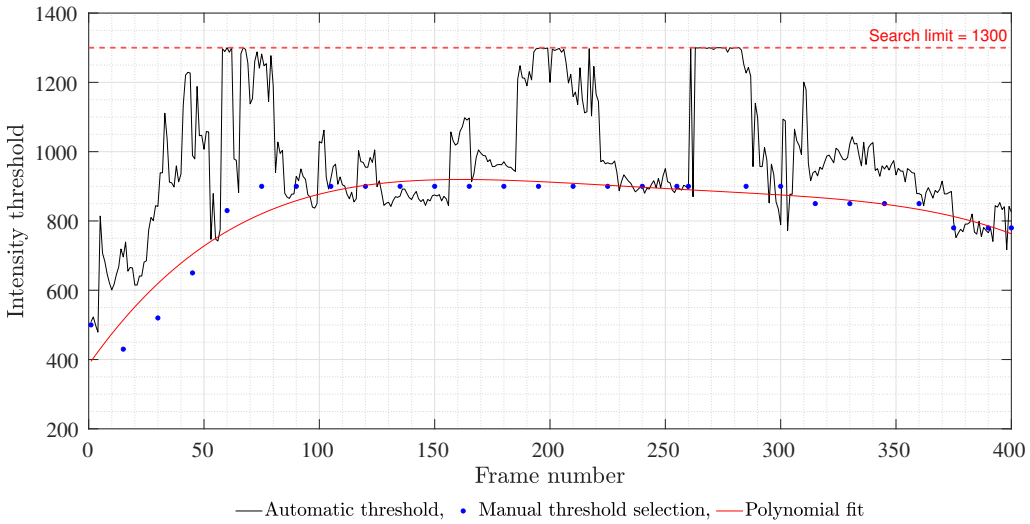

Figure 3.12: The intensity threshold as a function of frame number. The black line indicates the threshold that follows from the automatic threshold detection. The blue dots and the red line are the thresholds chosen based on visual inspection and polynomial fit, respectively. In the first 60 frames of the measurement, the same laser warm-up can be found as described in section 3.3 as well as the same decrease in intensity at the end of the measurement.

3.4.3. Conditional Vorticity

The edge detection aims to find the interface that separates the turbulent and non-turbulent regions. Analogous to the LIF measurement, where the concentration of dye separates the turbulent and non-turbulent regions, the vorticity field should show a similar picture. This is because the turbulent fluid is characterised by fluctuating vorticity [1], while the non-turbulent region is irrotational and does not carry vorticity. So, there should be a large difference in vorticity magnitude between the turbulent and non-turbulent regions. Therefore, the vorticity field is used to compare the different interfaces that result from the different threshold detection methods. The jet edges obtained from the edge detection methods are combined with the vorticity field to determine if the edge detection properly separates the turbulent and non-turbulent regions.

Vorticity calculation

The out-of-plane vorticity ω_z is obtained using the vorticity calculation method built into PIVWare. This program computes the vorticity in two steps. First, the velocity data is filtered using, [13]

$$\begin{aligned} \tilde{u}(i,j) &= \frac{1}{2}\left[u(i,j) + \frac{1}{2}\{u(i-1,j) + u(i+1,j)\}\right], \\ \tilde{v}(i,j) &= \frac{1}{2}\left[v(i,j) + \frac{1}{2}\{v(i,j-1) + v(i,j+1)\}\right]. \end{aligned} \tag{3.4}$$

The velocity data is filtered to suppress the measurement noise amplified by Equation 3.5, [13].

These filtered velocities are used for the second step, which involves using a second-order central differences scheme, shown in, [13]

$$\omega_z(i,j) \cong \frac{v(i+1,j) - v(i-1,j)}{2\delta x} - \frac{u(i,j+1) - u(i,j-1)}{2\delta y}. \tag{3.5}$$

In both Equations 3.4 and 3.5, i and j are the column and row index, respectively. Ref. [13] provides a more detailed description of this method.

Average conditional vorticity

The separation between regions is best shown by calculating the average conditional vorticity. This conditional profile shows the average amount of vorticity as a function of the distance from the interface as opposed to the mean vorticity as a function of the distance from a fixed position, i.e. the jet centreline. The jet edge obtained from the LIF edge detection methods is projected into the vorticity field to determine the average conditional vorticity. Vertical lines are drawn centered at the location of the interface as shown in Figure 3.13. The vertical lines are 16 pixels apart, which is the same as the resolution of the vorticity field. Ultimately, the conditional vorticity along these vertical lines is first scaled and then averaged to gain the average conditional vorticity of the frame.

The result from this procedure for frames 199, 240, and 264 can be found in Figures 4.10, 4.11, and 4.12. If the proper interface is identified, the conditional average should show zero vorticity outside the jet, followed by a sharp rise in vorticity at the interface.

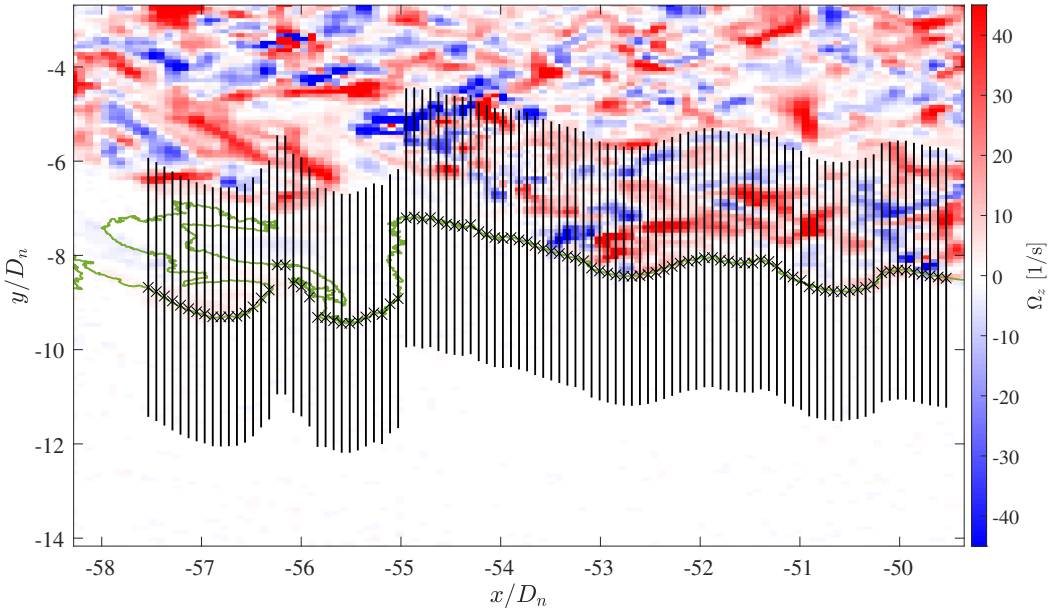

Figure 3.13: The vorticity field from frame 199. The interface from the manual edge detection is projected onto this field using green. The conditional vorticity is calculated along the vertical black lines, which extend $0.5 \cdot r_{1/2}$ from the interface in and out of the jet. The cross at each line marks the location of the interface. The distance between the lines is 16 pixels. For $x/D_n > -54$, the regions with and without vorticity are well separated by the interface. For $x/D_n < -54$, the interface is placed inside the non-turbulent region. This is most likely the result of velocity and, by extension vorticity, perpendicular to the light sheet that is transporting dye to this location.

4

Results

There are two sections on the measurement results of this experiment in this chapter. The first set of results come from the stationary measurements and are mainly used to validate the experimental design and to nondimensionalize the conditional vorticity obtained from the results of the measurements that move along with the edge of the jet. The second section discusses the moving measurements and is split into three parts. First, the PIV results of the moving measurements are shown. Next, the LIF edge detection is discussed. Finally, the PIV and edge detection results are combined to get the average conditional vorticity. The results from the moving measurements are the primary focus of this thesis.

Because of time constraints, only one of the moving experiments is analysed. This experiment is marked **Recording_Date 230320_Time=121746** in the experiment log. The first 59 frames of the moving measurement are not used for two reasons; see subsection 4.2.1. Important to note is that the flow direction is from right to left for all figures and the flow is taken in the direction of the negative x-axis.

4.1. Stationary measurements

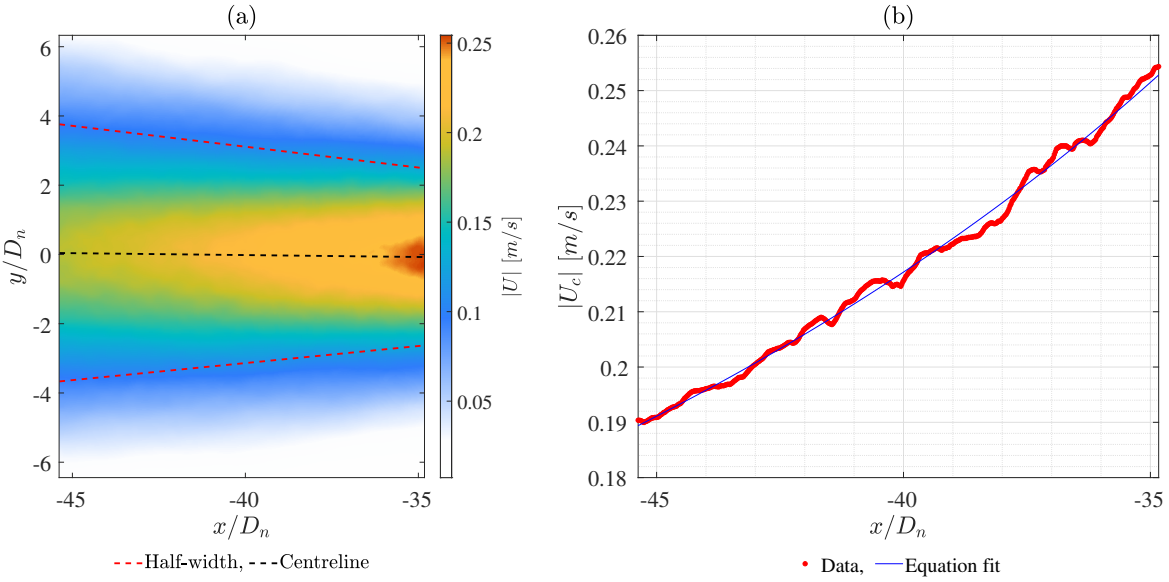

Figure 4.1: a) Average velocity magnitude in streamwise direction. The half-width and centreline are indicated with the dashed red and black lines, respectively. **b)** The centreline velocity from figure **(a)**. The measured data is displayed in red. Blue indicates the curve gained when the data is fitted to Equation 2.2.

For the stationary measurement, the centre of the FOV is set to $x = -40D_n$. At this location, 528 images are taken and averaged to reach the mean velocity field presented in Figure 4.1a. This scalar field is divided into vertical slices. The number of slices equals the number of data points along the x-axis. From each slice, the maximum velocity and its position are extracted. This is the centreline velocity. The centreline velocity is subsequently inverted to get the inverse centreline velocity. A straight line is fitted to the inverse centreline velocity to get the jet's decay constant and virtual origin. Instead of the inverse centreline velocity, Figure 4.1b shows the centreline velocity for an easier comparison of the result to the velocity contour in Figure 4.1a.

Next, the spreading rate of the jet is determined. The spreading rate follows from the half-width as a function of the downstream distance from the nozzle, which is found by noting the positions of the vectors with velocities equal to half of the centreline velocity. The spreading rate is the slope of a straight line fitted to these points. The values for the spreading rate, virtual origin, and decay constant can be found in Table 4.1. The average flow rate is converted to an average nozzle exit velocity using the nozzle diameter. These can also be found in Table 4.1.

U_n	D_n	$\frac{d}{dx}r_{1/2}$	$\lvert x_0\rvert/D_n$	B_u
$1.25 \pm 0.01\ m/s$	$10\ mm$	0.1095	3.35	6.63

Table 4.1: U_n and D_n are the nozzle exit velocity and nozzle diameter, respectively. Using these, the linear fit coefficients from the stationary measurement and Equations 2.1 and 2.2, the jet characteristics $\frac{d}{dx}r_{1/2}$, x_0 and B_u are derived. The position of the virtual origin is downstream of the nozzle.

Figure 4.2 shows the streamwise velocity profile, streamwise velocity root-mean-square (rms) fluctuation level, and Reynolds stress. These are compared to Case 5 from Ref. [6] and $x/D_n = 60$ from Ref. [7]. The former, in particular, is important because a slightly modified version of the same test setup is used. Moreover, the Reynolds number, nozzle diameter, and the nozzle geometry are similar. Therefore, these results should be comparable. The measurements from Ref. [7] were performed at $Re = 2 \times 10^3$. Figure 4.2 agrees with both references for the average velocity and Reynolds stress. However, the velocity fluctuations agree more with the data from Ref. [7] than with case 5 from [6]. It is expected for the rms velocity fluctuations to show two distinct peaks in the profile. These peaks are present in the data from Ref. [7] and the current experiment but not in the data from Ref. [6]. Despite these differences, the nondimensionalized profiles from Figure 4.2 are the same as those of a self-similar jet. The jet parameters are also within the expected range compared to those in Table 2.1.

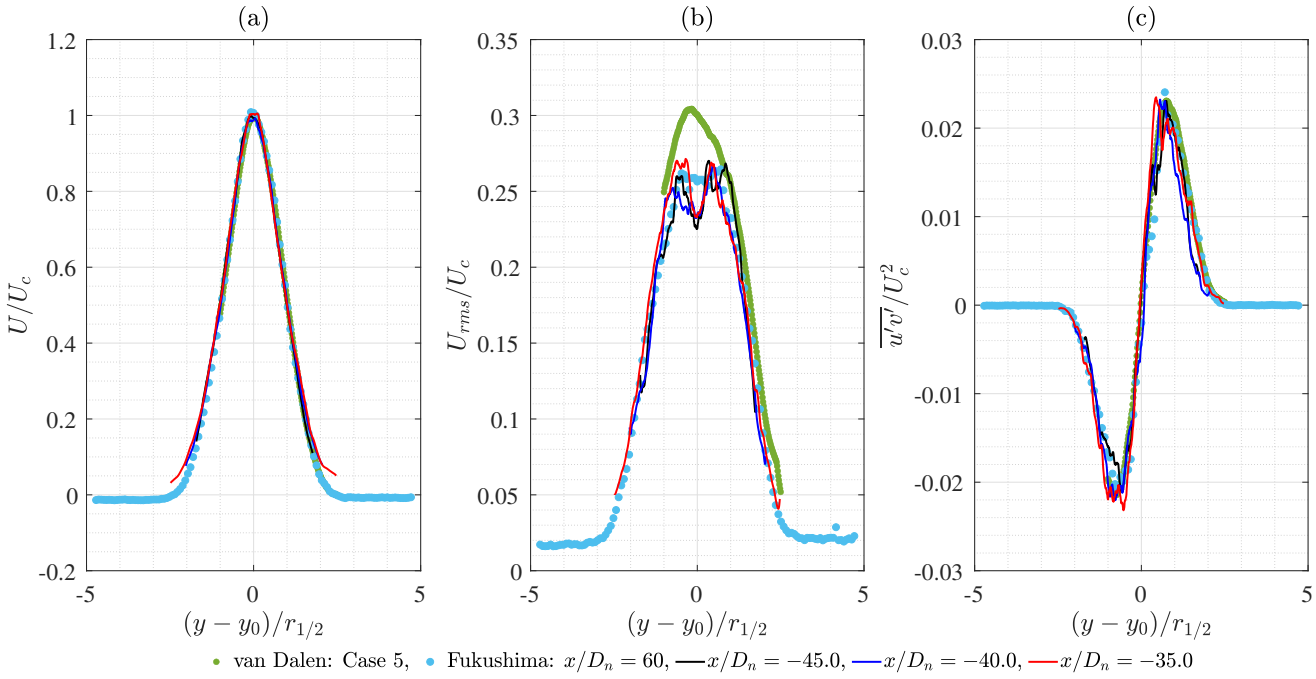

Figure 4.2: a) The scaled average velocity in the streamwise direction. **b)** The scaled velocity fluctuations in the streamwise direction. **c)** The scaled Reynolds stress. All figures show three positions of the current experiment as seen in Figure 4.1, data from Fukushima *et al.* [7] for $Re = 2 \times 10^3$, and Case 5 from van Dalen [6] for the same nozzle diameter and Reynolds number.

4.2. Moving measurements

4.2.1. PIV result

The first few seconds of the measurement have two challenges when it comes to the accuracy of the results. One of them is the laser warm up at the start of the measurement (see section 3.3). During the warm up period of the laser, the LIF calibration measurements, which relate the image intensity to the dye concentration, are not valid. The second challenge is the large in-plane particle displacement at the start of the measurement when the camera is close to the nozzle where the jet velocity is high. When looking at Figure 4.3, it can be seen that the percentage of spurious vectors consistently dips below five percent after frame 105. Even before frame 105, when the global percentage of spurious vectors is too high, almost all spurious vectors are found in the top part of the frame where the core of the jet resides. However, this experiment is focused on the turbulent/non-turbulent interface. Therefore, the density of spurious vectors around the TNTI is more important than the total fraction within the frame.

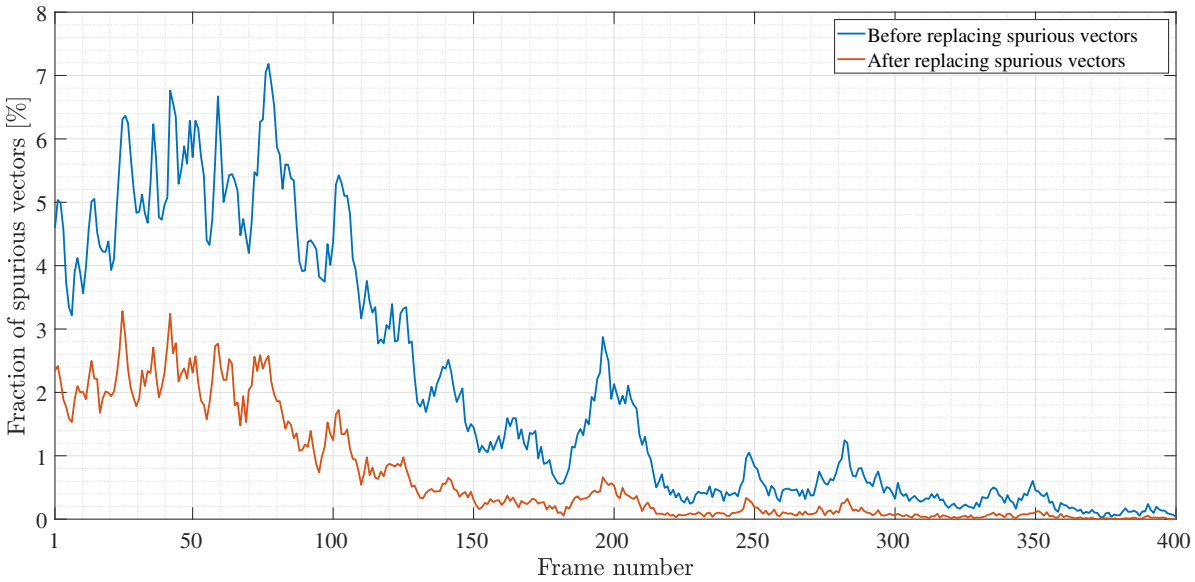

Figure 4.3: The fraction of spurious vectors in [%] as a function of frame number. It can be seen that the fraction of spurious vectors, before replacing, is consistently below 5% after frame 105. After replacing the spurious vectors, the outlier detection is used again to find the spurious vectors that were not recognised in the first pass.

The difference in spurious vector density is shown in Figure 4.4a. It shows the vector field on top of the LIF image for frame 60. The fraction of spurious vectors for the entire frame is above the threshold for a good PIV result, but, as stated before, most of these vectors are located in the core of the jet. This leaves the part close to the turbulent/non-turbulent region with a much lower density of spurious vectors. Therefore, this frame can still be used for analysing the turbulent/non-turbulent interface.

The results can be further improved by replacing the spurious vectors with an interpolated vector calculated using the surrounding good vectors. Figures 4.4 and 4.5 compare the vector fields before and after doing this. By replacing the spurious vectors, the fraction of spurious vectors in frame 60 decreases from 5.9% to 2.4% and most spurious vectors close to the TNTI have been replaced. However, it seems that many of the spurious vectors is the core of the jet were not recognised in the first pass. Frame 400 shows no further improvement to the result by replacing the spurious vectors. However, this is expected since the small displacements at the end of the experiment are easy to resolve with the given interrogation window size. This leaves room to improve the spatial resolution of the frame by decreasing the interrogation window size even further.

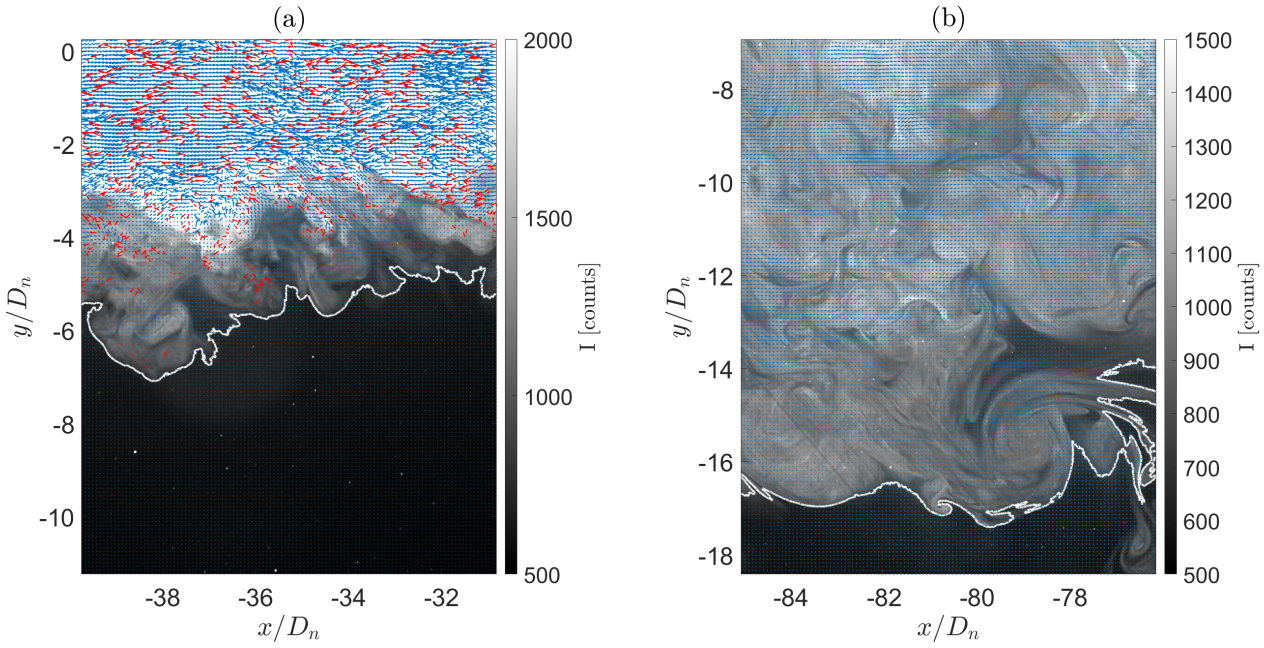

Figure 4.4: a) The vector field of frame 60. **b)** The vector field of frame 400. Both figures **(a)** and **(b)** show the vector fields before replacing the spurious vectors. The white line separates the turbulent and non-turbulent regions. Even before replacing the spurious vectors, the vector field frame 400 is almost devoid of spurious vectors.

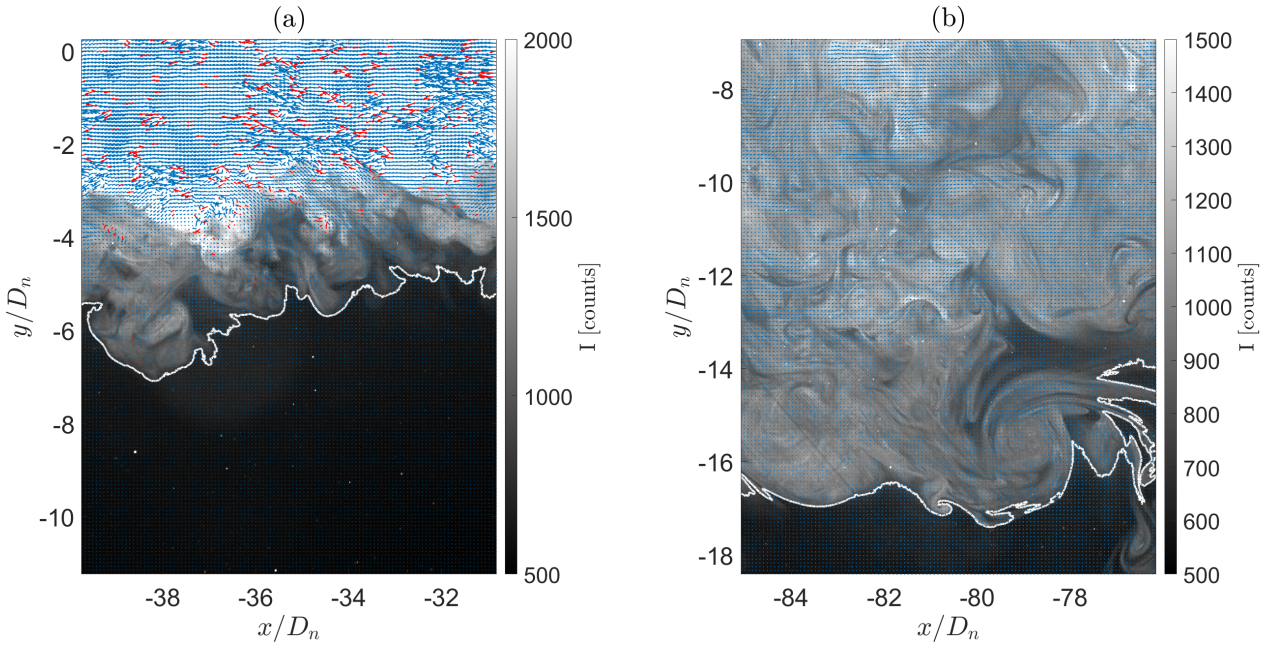

Figure 4.5: a) The vector field of frame 60. **b)** The vector field of frame 400. Both figures **(a)** and **(b)** show the vector fields after replacing the spurious vectors. The white line separates the turbulent and non-turbulent regions. Frame 400 is now entirely lacking any spurious vectors. The same cannot be said of frame 60. It is very clear that the core jet region of this frame is still not resolved correctly. However, close to the TNTI, the result has much improved.

4.2.2. Threshold detection

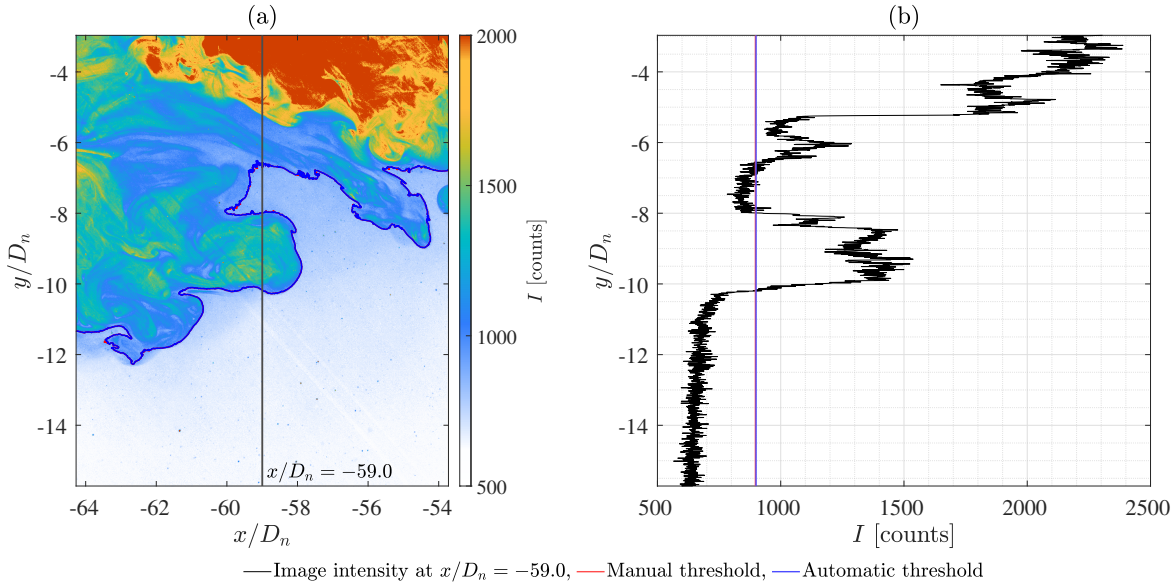

Figure 4.6: a) A comparison between the manual and automatic edge detection for frame 240. **b)** The LIF intensity as a function of y along the black line in **(a)**. The red and blue lines indicate the manual and automatic thresholds, respectively. The same colors are used in **(a)** to show the corresponding TNTI. The red lines are behind the blue lines, which makes them nearly impossible to see. This is the result of both methods finding similar intensity thresholds.

The first attempt of threshold detection is done using the automatic threshold detection algorithm described in subsection 3.4.2. There are frames where this algorithm succeeds in finding the right intensity threshold. An example of this can be seen in Figure 4.6. The frame nicely is split into two regions. The top part of the frames can be interpreted as the turbulent region and the bottom part as the non-turbulent region.

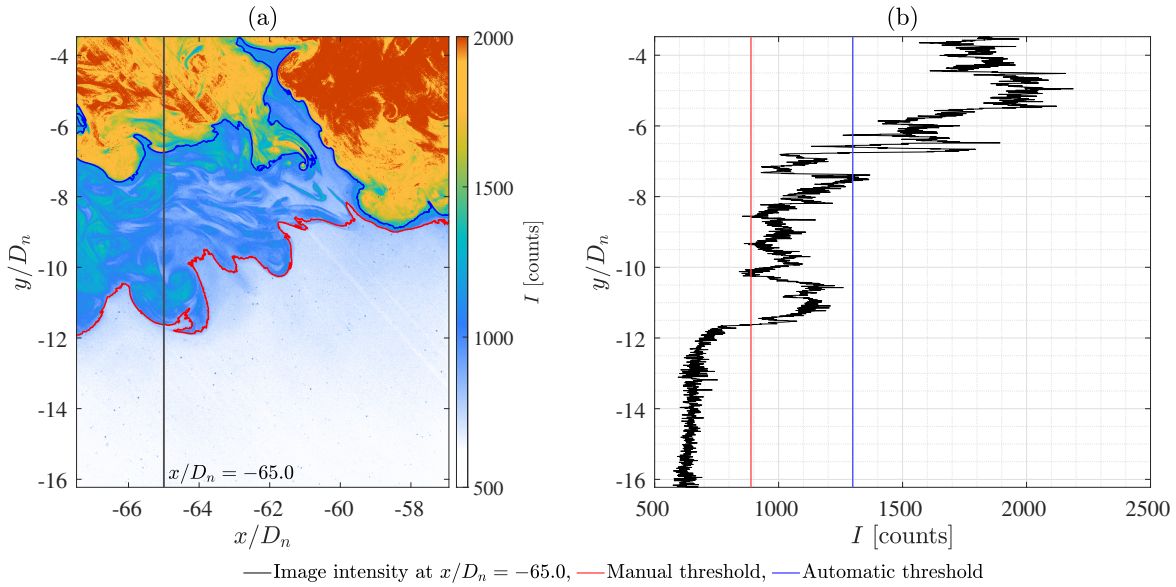

Figure 4.7: a) A Comparison between the manual and automatic edge detection for frame 264; also see Figure 3.12. **b)** The LIF intensity as a function of y along at the black line in **(a)**. The red and blue lines indicate the manual and automatic thresholds, respectively. The same colors are used in **(a)** to show the corresponding TNTI.

However, this method has difficulty detecting the intensity threshold corresponding to the outer boundary for many frames. One such frame can be seen in Figure 4.7, where the automatic edge detection method places the edge much further into the jet than expected. Adding the result from the manual edge detection splits the image into three instead of two regions. One region with fluid that has a high dye concentration, one with a low dye concentration, and finally, one with a dye concentration equal to the background.

These concentration zones show up again in the average intensity curves and are the core issue when it comes to choosing the intensity threshold. Figure 4.8 compares the average intensity and derivative average intensity curves from frames 240 and 264. The separation between the high and low concentration zones looks similar to the low and background concentration zones.

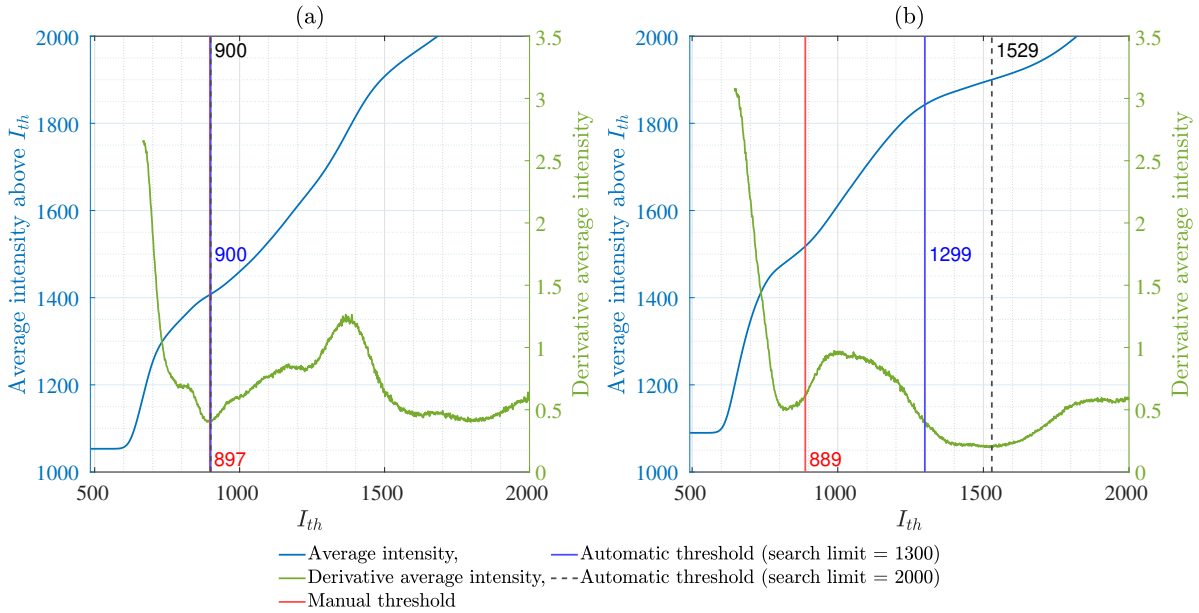

Figure 4.8: a) The average intensity and derivative average intensity corresponding to frame 240. **b)** The average intensity and derivative average intensity corresponding to frame 264. Three different thresholds are indicated with the vertical lines. A search limit is imposed to ensure the right threshold is found. For frame 240, both methods lead to similar thresholds. For frame 264, the manual and automatic threshold detection do not agree on a single threshold, leading to the difference in detected interfaces. Moreover, by increasing the original search limit from 1300 to 2000, an even higher threshold of 1529 is calculated (not shown in Figure 4.7).

Ideally, the local minimum, corresponding to the interface between the low and background concentration zones, is the absolute minimum of the curve. However, as Figure 4.8 shows, this is not true for many frames. Another approach would be to define the first local minimum in the derivative curve as the threshold. However, it is easy to find a frame where this is also not true. Looking at Figure 4.9, it can be seen that the threshold value corresponding to the first local minimum would result in an interface that is even further into the non-turbulent region than the interface from the manual detection method.

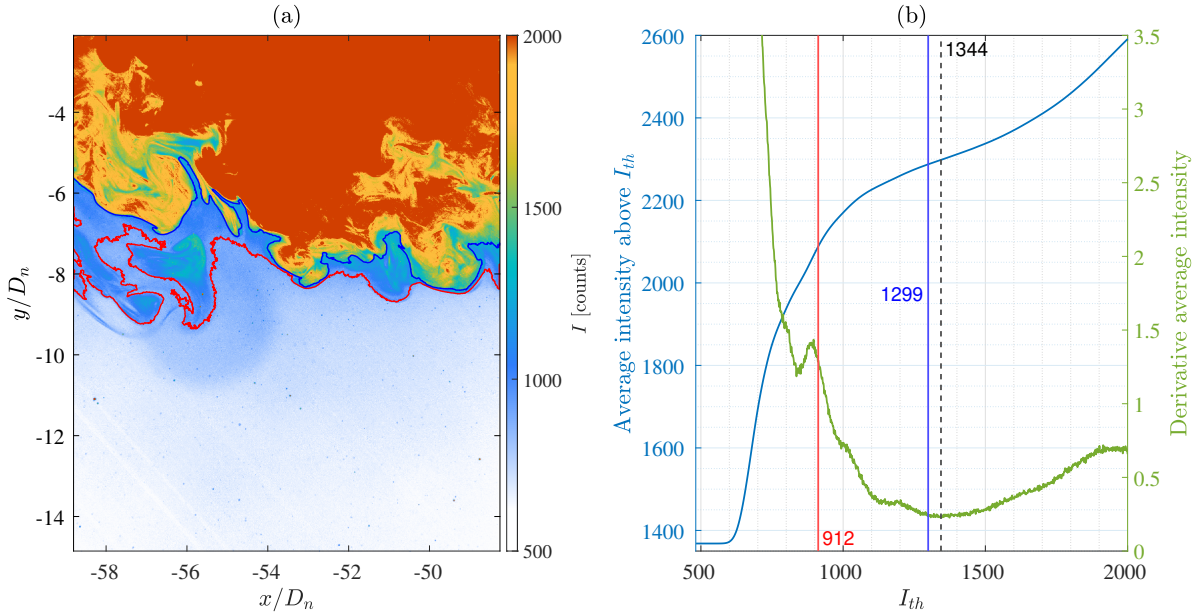

Figure 4.9: a) A comparison between the manual and automatic edge detection for frame 199; also see Figure 3.12. The red and blue lines indicate the manual and automatic thresholds, respectively. **b)** The average intensity and derivative average intensity corresponding to frame 199. Three different thresholds are indicated with the vertical lines. A search limit is imposed to ensure the right threshold is found. The manual and automatic threshold detection do not agree on a threshold leading to the difference in detected interfaces. Moreover, by increasing the original search limit from 1300 to 2000, an even higher threshold of 1344 is calculated. The colored vertical threshold lines from **(b)** correspond to the interfaces in **(a)**.

Figures 4.8 and 4.9 show the downside of applying an upper limit to the threshold value. If the limit is increased to 2000, the result of the automatic threshold detection changes to even higher threshold values. Therefore, a threshold value of 1299 such as in Figure 4.9, is not an actual threshold but an artifact of the search limit. For the search of the TNTI, this does not seem to be an issue because these thresholds exclude too much of the jet in almost every frame, and the imposed search limit of 1300 is already above the expected intensity threshold. The search limit could be made dependent on the average intensity of a frame. However, additional changes to the automatic edge detection algorithm are not pursued further in this research.

4.2.3. Average conditional vorticity

Frame average

Figures 4.10, 4.11 and 4.12 show the vorticity field and average conditional vorticity for frames 199, 240 and 264, respectively. The automatic detection from frame 199 seems to exclude a bit of vorticity from the turbulent region compared to the manual detection. Frame 240 shows good agreement between the two methods and the result looks about as expected, i.e. there is no vorticity outside the TNTI and a jump in vorticity at the interface.

The average conditional vorticity from frame 264 differs greatly from the other two. The manual edge detection may be too far into the non-turbulent region at some points, but the conditional average shows a good separation between the turbulent and non-turbulent regions. The automatic detection finds a completely different interface. Looking at the conditional average, it seems more like a turbulent/turbulent interface. There is low vorticity below the interface and high vorticity above the interface. It is clear that for this frame, the automatic edge detection method did not find the TNTI.

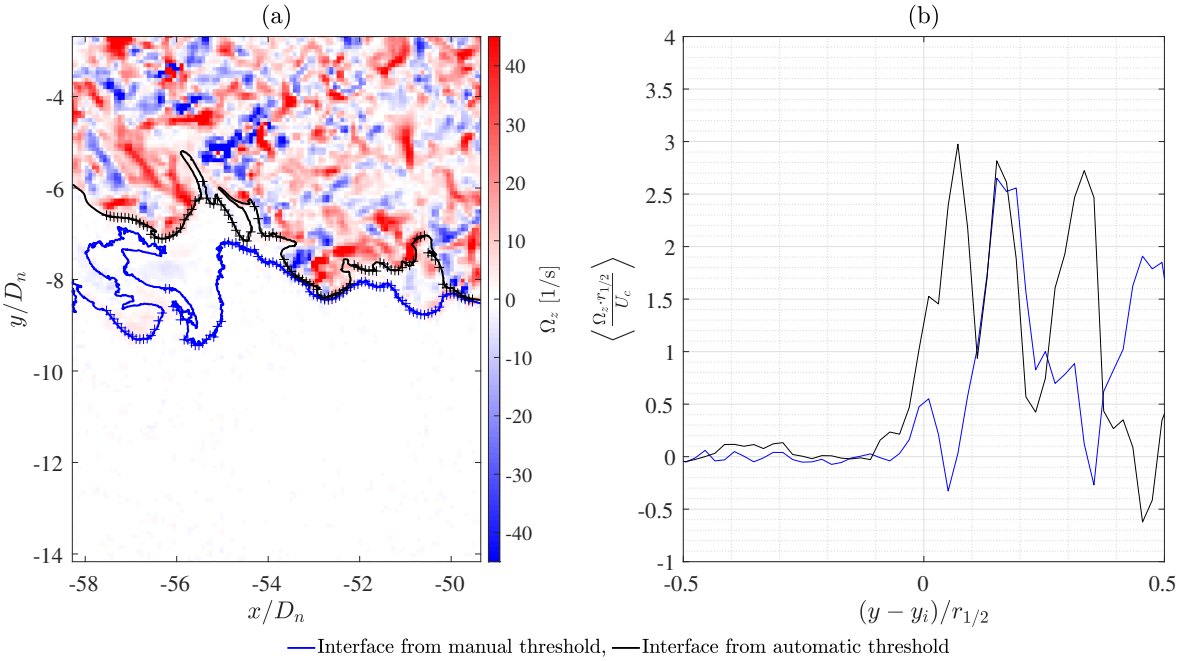

Figure 4.10: This figure shows the average conditional vorticity result for frame 199.**a)** The results from both the manual and automatic interface detection methods are placed on top of the vorticity field. **b)** The conditional vorticity average that results from the corresponding interface. The conditional average consists of 100 vertical lines, with zero being the location of the marked points on the edge. In both graphs, the blue line is the interface from the manual edge detection. The black line is the interface that results from the automatic edge detection. $0.5 \cdot r_{1/2} = 2.7 D_n$

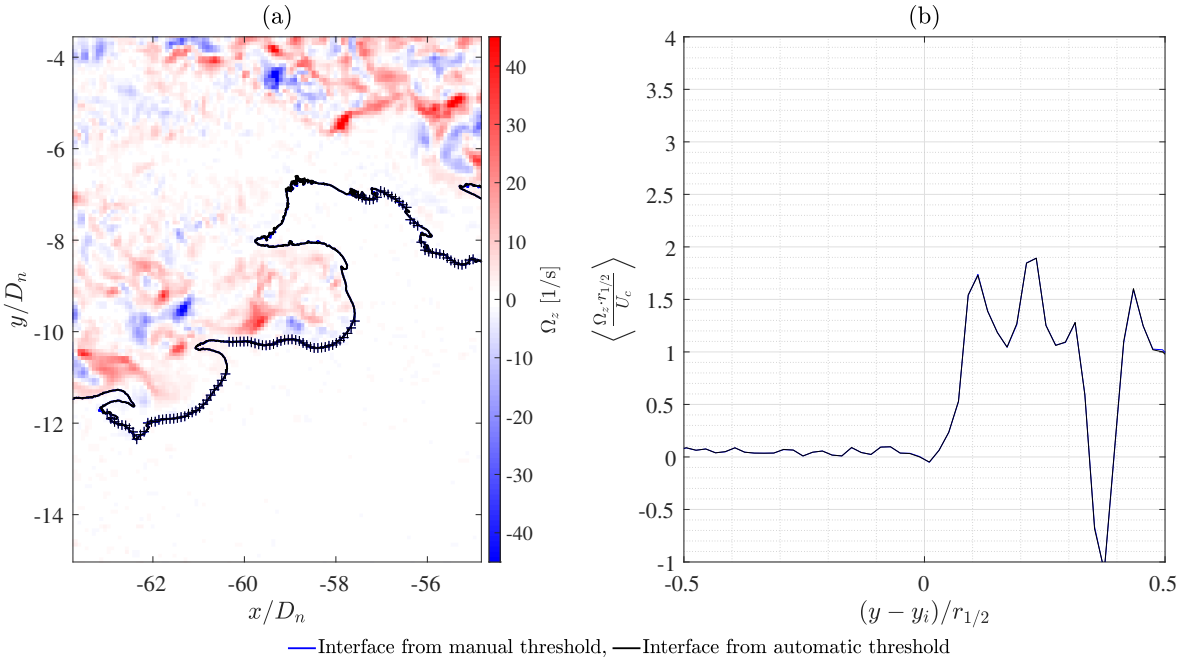

Figure 4.11: This figure shows the average conditional vorticity result for frame 240.**a)** The results from both the manual and automatic interface detection methods are placed on top of the vorticity field. **b)** The conditional vorticity average that results from the corresponding interface. The conditional average consists of 100 vertical lines, with zero being the location of the marked points on the edge. In both graphs, the blue line is the interface from the manual edge detection. The black line is the interface that results from the automatic edge detection. $0.5 \cdot r_{1/2} = 3.0 D_n$

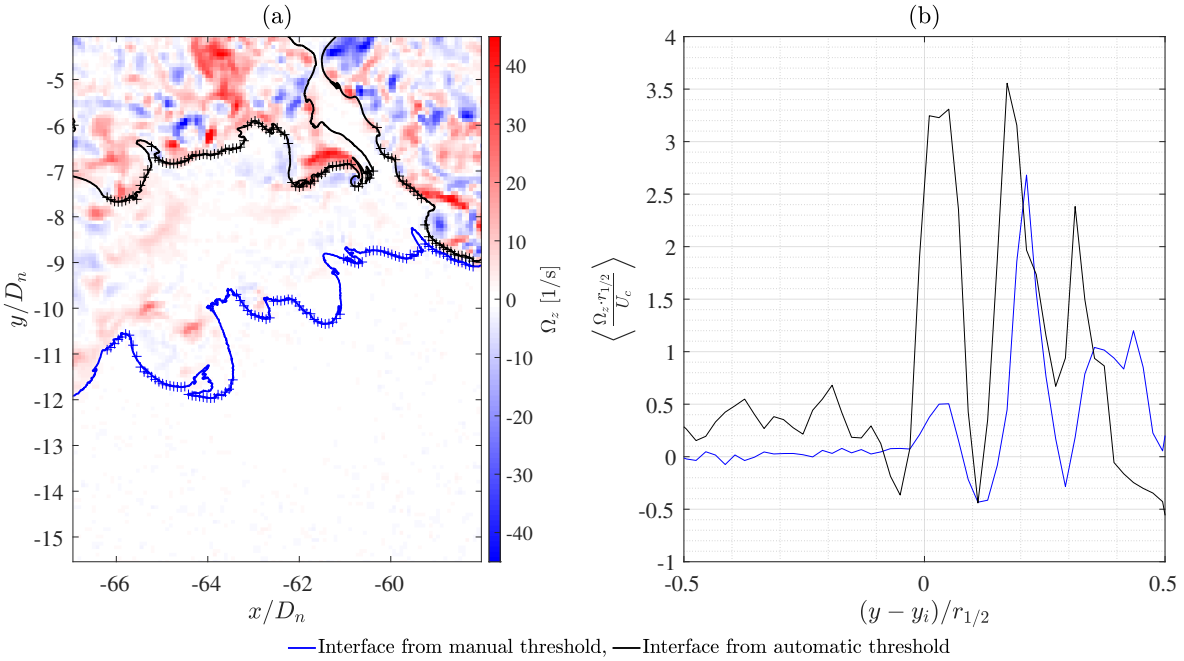

Figure 4.12: This figure shows the average conditional vorticity result for frame 264. **a)** The results from manual and automatic interface detection methods are placed on top of the vorticity field. **b)** The conditional vorticity average that results from the corresponding interface. The conditional average consists of 100 vertical lines, with zero being the location of the marked points on the edge. In both graphs, the blue line is the interface from the manual edge detection. The black line is the interface that results from the automatic edge detection. $0.5 \cdot r_{1/2} = 3.2 D_n$

Global average

Finally, the average conditional vorticity profiles from frame 60 to 400 are averaged to get the average conditional vorticity of the measurement. This result is shown in Figure 4.13. The automatic edge detection shows a far more pronounced peak with a shape similar to the literature at the interface location. Although, it also includes more vorticity in the non-turbulent region compared to manual edge detection. Both results also show negative vorticity outside of the interface. However, this is due to the inclusion of interpolated vorticity outside of the frame and should be ignored.

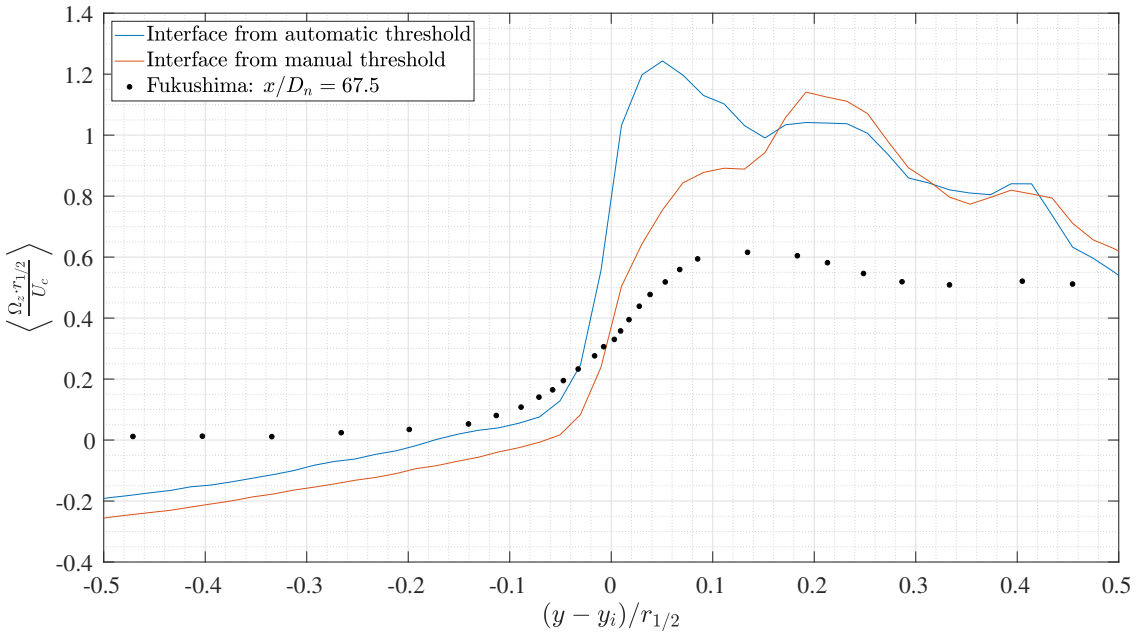

Figure 4.13: The average conditional vorticity result from both interfaces is compared. This conditional average is calculated from frames 60 to 400. Additionally, the conditional vorticity profile from [4] is added as a point of comparison.

5

Conclusions & Recommendations

5.1. Conclusions

This thesis describes a method for measuring the TNTI of an axisymmetric jet with a co-moving camera system. These measurements cover three Reynolds numbers, approximately equal to 9×10^3, 1.2×10^4, and 3.1×10^4, over a distance of approximately 60 nozzle diameters. For these measurements, PIV is used to measure the velocities and LIF is used to detect the TNTI, while an additional camera was deployed to measure the light intensity of the laser. One measurement of $Re \approx 1.2 \times 10^4$ is processed to get insight into the quality of the results that can be obtained by such a measurement. This measurement consists 400 frames and for each there are two PIV measurements, two LIF measurements, and one laser intensity measurement.

The laser intensity measurements shows that the light output of the laser is slowly increasing during the measurement and that the laser intensity fluctuations are found to be within the specification of the laser. So, pulse-to-pulse variation is not considered an issue for the LIF results.

The camera system moves at a constant velocity for all measurements. However, this is not ideal as the interface moves faster at the beginning of the measurement compared to the end of the measurement. Although it is not quantified, there are measurements that show the system is able to track the interface evolution for a large part of the measurement domain. The field of view is also constant throughout the measurement. At the beginning of the measurement, the FOV is much larger than needed to capture engulfment events. At the end of the measurement, the FOV is slightly too small, and the TNTI is lost in a few frames after $x/D_n > 76$.

For this experiment, a laser with a fixed exposure time delay is used. This results in large particle displacements close to the nozzle. The combination of a large FOV and large particle displacements at the beginning of the measurement requires large interrogation windows and leads to low spatial resolution for this part of the measurement domain. It is estimated that the spatial resolution for the experiment shown varies between approximately 20η and 6η from beginning to end, respectively.

The custom multigrid interrogation works well when it comes to resolving the large particle displacements for most of the measurements. Only at the very beginning of the measurement there appears to be too many spurious vectors in the region close to the TNTI. After frame 60, most of the spurious vectors close to the TNTI can be replaced without difficulty. After frame 100, the total fraction of spurious vectors is below 5% and parts closer to the core of the jet can also be fully resolved.

The automatic LIF edge detection can not reliably detect the turbulent/non-turbulent interface and would, occasionally, detect an interface internal to the jet instead. This can be seen in 3.4.2 showing the LIF image intensity, where the threshold value is not always at the expected first jump. This behaviour is attributed to the existence of multiple discrete levels in dye concentration and resulting inflection points in the average intensity curves.

The average conditional vorticity results also show levels in the vorticity magnitude when compared to a manually determined interface and support the conclusion drawn from the LIF edge detection that an internal interface is detected on occasion.

5.2. Recommendations

As stated before, the camera system can follow the interface evolution for a large section of the measurement domain and is able to make high resolution instantaneous measurements in this section. However, there are still improvements to be had in the experimental setup and the data processing to fully achieve the goal set at the beginning of the thesis.

First of all, the constant camera movement could not follow the same part of the TNTI throughout the entire measurement domain due to the changing interface velocity during the measurement. Progressively slowing the camera movement during the measurement could solve this. However, it will be more difficult to correct the camera movement in the PIV results, and the position of the camera system will need to be monitored during the measurement.

This experiment would also benefit from a laser with a variable exposure time delay to decrease the particle displacements at the beginning of the experiment and could allow for smaller interrogation regions. This will improve the spatial resolution of the measurement and allow for easier processing of the velocity measurements. The smaller particle displacements will also make it easier to resolve the velocities in the core of the jet. If the variable exposure time delay laser is combined with a smaller FOV at the start of the experiment that is slowly increased by moving the camera away from the laser sheet while moving downstream, it can improve the spatial resolution at the beginning of the measurement without changing the interrogation window size.

For future experiments that also use a pulsed laser, the flash lamps of the laser should also receive triggers during the movement back to the start of the experiment and while waiting at the starting position. This ensures the laser cavities stay at their operational temperature, which keeps the output light intensity more constant.

Further research can look into different edge detection methods, either using a different method to compute the threshold value for the scalar field or to get the TNTI directly from the velocity measurements. Getting the TNTI directly from the velocity measurements removes not only the need for the additional measurement method but also the need to measure the pulse-to-pulse variance. Thus, eliminating two cameras.

Removing the LIF and laser intensity measurement frames also creates room in the acquisition computers memory to record more PIV frames. These extra PIV frames can used to measure slower moving flows, increase the size of the measurement, or increase the frame rate for high velocity measurements.

Future research can also look into the internal interfaces and whether the mechanisms that govern the TNTI also apply to those.

References

[1] F. T. Nieuwstadt, B. J. Boersma, and J. Westerweel, *Turbulence: Introduction to theory and applications of turbulent flows*. Springer, 2016.

[2] C. B. da Silva, J. C. Hunt, I. Eames, and J. Westerweel, "Interfacial layers between regions of different turbulence intensity," *Annual Review of Fluid Mechanics*, vol. 46, no. 1, pp. 567–590, 2014. DOI: 10.1146/annurev-fluid-010313-141357.

[3] J. Mathew and A. J. Basu, "Some characteristics of entrainment at a cylindrical turbulence boundary," *Physics of Fluids*, vol. 14, no. 7, pp. 2065–2072, 2002. DOI: 10.1063/1.1480831.

[4] J. Westerweel, C. Fukushima, J. M. Pedersen, and J. C. Hunt, "Momentum and scalar transport at the turbulent/non-turbulent interface of a jet," *Journal of Fluid Mechanics*, vol. 631, pp. 199–230, 2009. DOI: 10.1017/s0022112009006600.

[5] B. J. Boersma, G. Brethouwer, and F. T. Nieuwstadt, "A numerical investigation on the effect of the inflow conditions on the self-similar region of a round jet," *Physics of Fluids*, vol. 10, no. 4, pp. 899–909, Oct. 1998. DOI: 10.1063/1.869626.

[6] L. E. van Dalen, "The turbulent/non-turbulent interface of a round jet.," M.S. thesis, Delft University of Technology, 2022.

[7] C. Fukushima, L. Aanen, and J. Westerweel, "Investigation of the mixing process in an axisymmetric turbulent jet using piv and lif," *Laser Techniques for Fluid Mechanics*, pp. 339–356, 2002. DOI: 10.1007/978-3-662-08263-8_20.

[8] H. J. Hussein, S. P. Capp, and W. K. George, "Velocity measurements in a high-reynolds-number, momentum-conserving, axisymmetric, turbulent jet," *Journal of Fluid Mechanics*, vol. 258, pp. 31–75, 1994. DOI: 10.1017/s002211209400323x.

[9] N. R. Panchapakesan and J. L. Lumley, "Turbulence measurements in axisymmetric jets of air and helium. part 2. helium jet," *Journal of Fluid Mechanics*, vol. 246, pp. 225–247, 1993. DOI: 10.1017/s0022112093000102.

[10] W. Rodi, "A new method of analyzing hot wire signals in highly turbulent flow and its evaluation in a round jet.," *DISA Information 17*, 1975.

[11] I. Wygnanski and H. Fiedler, "Some measurements in the self-preserving jet," *Journal of Fluid Mechanics*, vol. 38, no. 3, pp. 577–612, 1969. DOI: 10.1017/s0022112069000358.

[12] K. Iwano, J. Hosoi, Y. Sakai, and Y. Ito, "Power spectrum of high Schmidt number scalar in a turbulent jet at a moderate reynolds number," *Experiments in Fluids*, vol. 62, no. 6, 2021. DOI: 10.1007/s00348-021-03216-5.

[13] R. J. Adrian and J. Westerweel, *Particle image velocimetry*. Cambridge University Press, 2011.

[14] J. Westerweel, T. Hofmann, C. Fukushima, and J. Hunt, "The turbulent/non-turbulent interface at the outer boundary of a self-similar turbulent jet," *Experiments in Fluids*, vol. 33, no. 6, pp. 873–878, Jan. 2002. DOI: 10.1007/s00348-002-0489-5.

[15] R. R. Prasad and K. R. Sreenivasan, "Scalar interfaces in digital images of turbulent flows," *Experiments in Fluids*, vol. 7, no. 4, pp. 259–264, Feb. 1989. DOI: 10.1007/bf00198005.